



# Ni-based catalysts supported on acid/alkali-activated coal fly ash residue for improved glycerol steam reforming

Kang Gao, Ommolbanin Alizadeh Sahraei, Maria C. Iliuta\*

Department of Chemical Engineering, Université Laval, Québec QC G1V 0A6, Canada



## ARTICLE INFO

**Keywords:**  
Glycerol steam reforming  
Hydrogen  
Coal fly ash  
Acid/alkali treatment  
NiFe alloy

## ABSTRACT

Application of coal fly ash (FA) residues as catalyst support is mainly restricted because of low surface area and high sulfur content. In the present work, the physicochemical properties of a low-efficiency FA were significantly improved via simple acid/alkali treatments consisting of one-step ( $\text{HNO}_3$  or  $\text{NaOH}$ ) or two-step ( $\text{NaOH}/\text{HNO}_3$  or  $\text{HNO}_3/\text{NaOH}$ ) leaching-partial-dissolution (LPD). As a result, as compared to Ni-FA, the catalytic activity of the Ni-FA(treated) catalysts for glycerol steam reforming was considerably enhanced. Alkali-LPD is more effective than acid-LPD in simultaneously improving FA's surface area and regulating FA's elemental distribution. Ni-FA ( $\text{HNO}_3/\text{NaOH}$ ) has the best performance with high glycerol conversion to gas (99.2%) and  $\text{H}_2$  yield (74.5%), attributed to *i*) removal of sulfur-containing species by acid-LPD, *ii*) upgrading specific surface area, iron-exposure, and Ni dispersion via alkali-LPD, *iii*) diminishment of coke using acid/alkali-LPD sequence treatment, and *iv*) enhancement of catalytic stability due to the formation of NiFe alloys.

## 1. Introduction

Hydrogen is well acknowledged as the main clean energy carrier for achieving pollution-free and zero-carbon emissions. Currently, the development of various fuel cells would provide feasibility routes for its wide application in many fields. Catalytic steam reforming (SR) as the mature  $\text{H}_2$  production approach is one of the most promising technologies in combination with fuel cells. In particular, the glycerol steam reforming (GSR) for green  $\text{H}_2$  production is increasingly drawing the attention of the scientific community [1–3], especially because *i*) the stoichiometric  $\text{H}_2$  formation is higher compared to other feedstocks (methane, ethanol, acetic acid, phenol, bio-oil, etc.) and *ii*) the valorization of glycerol (waste-to- $\text{H}_2$ ) increases the commercial competitiveness of  $\text{H}_2$ /biodiesel application, satisfying a sustainable development.

Catalyst, as a pivotal material, has a strong impact on the selectivity and yield of  $\text{H}_2$ , and has long been a research hotspot associated with improving its cost-performance ratio. Among the limited number of active metal catalytic candidates (noble and transition metals), Ni has been commonly employed in steam reforming due to its *i*) high efficiency for C-C, C-H, and O-H rupture, *ii*) favorable effect on water gas shift (WGS) reaction, *iii*) high availability, and *iv*) cost-effectiveness. As a result, discovering and/or exploiting more diversified and sustainable carrier materials (support) that improve the price-performance of the

catalyst have attracted a great deal of attention from academics and the government [4–8]. In this context, recycling and valorizing different kinds of wastes and residues are increasingly considered to generate energy and added-value products. This approach could bring additional industrial-economic revenue, diminish environmental and health hazards, and reduce environmental protection costs. Meanwhile, the sustainable utilization of the waste and residues could alleviate the energy requirements for industrial processing, which is desirable considering the depletion of finite/nonrenewable resources, and prevent the inevitable environmental degradation. Certainly, the residues from coal-fired industries have been increasing due to overreliance on coal resources over the last century [9–11]. These solid residues could be used as potential support materials for catalysis.

Coal fly ash (FA) as the main coal-fired solid residue (85–95 wt%) is annually generated with 750 million tonnes in worldwide thermal power plants, and the subsequent dumping causes serious environmental problems. FA has recently been employed in sorption and catalysis because of its superior thermal stability, in addition to soil amelioration, construction, ceramic, geopolymers, zeolite synthesis, and valuable elements recovery [9,11–14]. Several works applied FA as support in catalytic reforming for  $\text{H}_2$  production [15–22]. Wang et al. stated that the wet impregnation of Ni into FA displayed a significant rise in the catalytic activity for bio-oil model compounds (acetic acid and

\* Corresponding author.

E-mail address: [maria-cornelia.iluta@gch.ulaval.ca](mailto:maria-cornelia.iluta@gch.ulaval.ca) (M.C. Iliuta).

phenol), whose SR performances were very close to those of commercial Ni-based catalysts [16–18]. The authors also found that the presence of alumina, alkali and alkaline earth metal oxides (AAEMs), and iron oxides within FA not only acted as support beneficial for Ni active phase dispersion, but also participated in the SR reaction by cracking reactants. However, Zhou et al. found that FA is not a good catalytic candidate in methane reforming and partial oxidation in comparison to coal char (larger surface area) [22]. To unravel the suitability of FA as catalytic support, four kinds of FA originated from different thermal power plants (Canada, India, and China) were chosen in our previous work to develop Ni-FA reforming catalysts and investigate their application in glycerol steam reforming (GSR) [15]. We found that not all kinds of as-received FA materials are suitable as support and demonstrated that the catalytic activity of Ni-FA catalysts synthesized by the solid-state impregnation is substantially influenced by the physicochemical and mineralogical properties of FA. This was strongly dependent upon the types of coal and the conditions at which they were generated. It was determined that the AAEMs inside the studied FA were ineffective for enhancing the WGS reaction. Moreover, a higher specific surface area, the presence of specific structure crystals (nepheline), and a low amount of sulfur/calcium-containing species offer to the developed catalyst a better efficiency (selected FA could provide a high hydrogen yield of 78.8%). However, most FA present low specific surface area and an increased content of calcium/sulfur due to the flue gas desulfurization process during coal combustion [23]. Considering FA's diversity, complexity, and heterogeneous character, how to modify low-activity FA via an easy approach to fulfill the catalytic reforming for green H<sub>2</sub> production is an interesting and challenging topic.

To increase the specific surface area and remove impurities of as-received FA, both mechanical and chemical pretreatments could be implemented, such as heating/crushing activation and acidic/basic solution leaching [20,21,24]. Lu et al. employed wet impregnation to synthesize Ni- and Ni-Co- catalysts supported on the activated FA (thermal treatment followed by 2 mol•L<sup>-1</sup> HNO<sub>3</sub> washing for various durations) for toluene steam reforming [20]. The results showed that 6 h HNO<sub>3</sub> treated FA-supported 20 wt% Ni-based catalysts exhibited the best catalytic behavior, possibly owing to the formation of Fe<sub>0.94</sub>Ni<sub>0.06</sub> alloy. Partly substituting Ni with Co resulted in superior catalytic performance. Furthermore, Gao et al. prepared 10 wt% Ni-based catalysts via the wet impregnation of alkali-treated or alkali/acid (25 wt% NaOH and 2 mol•L<sup>-1</sup> HNO<sub>3</sub>) co-treated FA for syngas production by biogas dry reforming [21]. The catalyst using co-treated FA as support exhibited the best catalytic activity, with high CH<sub>4</sub> and CO<sub>2</sub> conversion (> 95%), and thermal stability at 850 °C for 12 h, owing to the improvement in surface area and pore volume. Overall, chemically treated FA as support applied in catalysis was found to exhibit satisfying catalytic activity, which was closely associated with its structure and composition. Nevertheless, these experiments did not elucidate the dissolution behavior of FA during acid/alkali treatment, its relationship with structural changes, and the final catalytic activity. Therefore, additional and thorough characterization approaches need to be carried out to clarify the discrepancy of reported treatments in respect to the physicochemical characteristics of the prepared supports and catalysts. In addition, we propose the hypothesis that the treatment sequence (acid/alkali or alkali/acid) may alter the FA's texture and subsequently affect the catalytic performance of FA-supported catalysts.

In this context, the present work aims to fill the gaps mentioned above. We attempted to significantly improve a low efficiency FA (as support for Ni-based catalyst) by regulating its physicochemical properties via simple acid/alkali treatments consisting in one-step (HNO<sub>3</sub> or NaOH) or two-step (NaOH/HNO<sub>3</sub> or HNO<sub>3</sub>/NaOH) leaching-partial-dissolution (LPD). For the first time, a comprehensive comparison of FA dissolution behavior in acid/alkali treatments and the introduction of two-step LPD with different operation sequences, as well as the evaluation of the catalytic activity of the developed FA-supported catalysts, were examined here. The FA was chosen based on our previous

work where the corresponding FA-supported Ni-based catalyst (15% Ni-FA1) showed very low glycerol conversion to gas products (53%) and H<sub>2</sub> yield (21%) compared to the best one (93% and 77%) [15]. The effect of investigated treatments, including one-step and two-step LPD, on the properties of FA as catalytic support was first systematically characterized by means of N<sub>2</sub> adsorption-desorption, XRF, XRD, SEM, and H<sub>2</sub>-TPR techniques. Thereafter, these treated FA were applied to develop Ni-FA catalysts and thoroughly evaluate their performance in GSR through quantitative/qualitative analysis of gaseous and liquid products (glycerol conversion and yield of gaseous products). To rationalize the correlation between the physicochemical characteristics of the synthesized Ni-FA catalysts and their catalytic performance, several characterization techniques including N<sub>2</sub> adsorption-desorption, SEM, XRD, H<sub>2</sub>-TPR, TEM, XPS, and H<sub>2</sub>-pulse chemisorption analysis were carried out on fresh and reduced synthesized catalysts. Moreover, the used catalysts (associated with structure change, coke deposition, and sintering) were thoroughly characterized using N<sub>2</sub> adsorption-desorption, XRD, TEM, TGA/DTG, *in-situ* TPO, and Raman analysis.

## 2. Experimental section

### 2.1. Material preparation

Coal fly ash (FA) was collected from Lakeview generating station (coal-burning electric power plant) located in Ontario, Canada. Before preparing the catalyst, as-received FA was calcined, to remove the organic (combustible) components, at 800 °C for 2 h in air flow at the rate of 10 °C•min<sup>-1</sup>. Hereafter, four chemical procedures (alkali, acid, alkali/acid, and acid/alkali treatments) were carried out to stimulate the activity of the calcined FA. (i) One-step alkali-LPD: 5.0 g NaOH was first dissolved into 15 mL deionized water in a flask coupled to a reflux condenser and equipped with a magnetic stirrer; NaOH solution (25 wt %) was stirred and heated up to 95 °C; 5.0 g of calcined FA (NaOH/FA mass ratio of 1:1) was thereafter added into the designed NaOH solution while maintaining stirring for 30 min at 95 °C; subsequently, the suspension was separated by filtration and the filter cake was thoroughly washed with deionized water; hereafter, the filter cake was dried in the oven at 105 °C for 12 h, and designated as FA<sup>Na</sup>. (ii) One-step acid-LPD: 5.0 g of calcined FA was added to 50 mL of a 2 M HNO<sub>3</sub> aqueous solution (100 g•L<sup>-1</sup>); the mixture was then stirred at room temperature for 30 min; the filtration and drying processes were similar to the alkali-LPD process; the dried solid slag was designated as FA<sup>H</sup>. (iii) Two-step co-treatment: the obtained FA<sup>Na</sup> and FA<sup>H</sup> were further treated according to the one-step acid-LPD and one-step alkali-LPD, respectively, and were labeled as FA<sup>Na/H</sup> and FA<sup>H/Na</sup>. The possible reactions during acid and alkali treatment are listed in Table S1.

Subsequently, FA-supported catalysts with 7.5 wt% Ni loading were synthesized according to our previous study [15]. Approximately 2.0 g of designed (treated) FA support was mixed with 0.8 g of nickel nitrate hexahydrate (Ni(NO<sub>3</sub>)<sub>2</sub>•6H<sub>2</sub>O) via solid-state impregnation method (SSI). Acetone was simultaneously used to homogenize the mixture and gradually evaporated during grinding. The grinded mixtures were dried at 80 °C for 12 h. The as-constructed catalysts were then heated at 600 °C for 5 h in air stream of 100 mL•min<sup>-1</sup>. Finally, the calcined catalysts were crushed and sieved to particle size less than 100 µm. The FA-supported 7.5 wt% Ni-based catalysts used herein are labeled as Ni-FA and Ni-FA<sup>x</sup>, where x (Na, H, Na/H, and H/Na) refers to the corresponding treatment procedure: NaOH, HNO<sub>3</sub>, NaOH/HNO<sub>3</sub>, and HNO<sub>3</sub>/NaOH. Except where indicated, the alkali-LPD FA<sup>x</sup> appeared in the present work refers to the FA<sup>Na</sup>, FA<sup>Na/H</sup>, and FA<sup>H/Na</sup> samples. Acid-LPD FA<sup>x</sup> refers to FA<sup>H</sup>, FA<sup>Na/H</sup>, and FA<sup>H/Na</sup> samples.

### 2.2. Characterizations

#### 2.2.1. N<sub>2</sub> adsorption-desorption analyzer

N<sub>2</sub> adsorption-desorption isotherms of supports and synthesized

catalysts were obtained by a Micromeritics Gemini VII (2390) apparatus at  $-196^{\circ}\text{C}$  to acquire their texture information. Prior to measurements, all samples were degassed at  $300^{\circ}\text{C}$  for 4 h to remove all impurities (moisture and gas), then gradually cooled to room temperature under the  $\text{N}_2$  stream. The specific surface area was measured from the adsorption isotherm using Brunauer-Emmet-Teller (BET) method in the relative pressure ( $p/p^*$ ) range of 0.05–0.3. Pore size distribution and cumulative volumes of pores were obtained from desorption branches of  $\text{N}_2$  isotherms.

#### 2.2.2. X-ray fluorescence spectrometer

The chemical compositions of FA and  $\text{FA}^x$  were determined by Rigaku ZSX primus X-ray fluorescence (XRF) spectrometer (Rigaku Corporation Tokyo, Japan). Prior to analysis, 0.5 g of powder was tabulated (10 mm  $\times$  3 mm) at 50 Mpa with ceridust as matrix binder material (mass ratio FA : ceridust = 10 : 3). Each sample was then subjected to a full range scan to measure all detectable elements and the results were reported as oxides ( $\text{Al}_2\text{O}_3$ ,  $\text{SiO}_2$ ,  $\text{Fe}_2\text{O}_3$ ,  $\text{CaO}$ ,  $\text{Na}_2\text{O}$ ,  $\text{MgO}$ ,  $\text{K}_2\text{O}$ ,  $\text{P}_2\text{O}_5$ ,  $\text{TiO}_2$ ,  $\text{MnO}$ ,  $\text{SO}_3$ ,  $\text{Cr}_2\text{O}_3$ , and  $\text{SrO}$ ). The results were also normalized to 100% weight content.

#### 2.2.3. X-ray diffractometer

X-ray diffraction (XRD) patterns analysis was performed in the PANalytical AERIS benchtop X-ray diffractometer to identify the crystalline phases. The beam voltage and current used in the instrument were set to 40 kV and 40 mA, respectively, along with a secondary monochromator using Cu-K $\alpha$  radiation at a wavenumber of 0.1542 nm. XRD patterns were recorded in 20 values range from  $5^{\circ}$  to  $80^{\circ}$  at a ramping rate of  $2^{\circ}/\text{min}$ . In addition, the Scherrer equation was used to calculate the average crystal size of the active metal phases for reduced and used catalysts from the XRD pattern.

#### 2.2.4. Scanning electron microscopy

The surface morphology of the samples was captured using a scanning electron microscope (SEM-VEGA3) via a retractable solid state backscattered electron (BSEs) detector. The working distance of the SEM was 8 mm, with a 15.0 kV accelerating voltage and a 10 A beam current. Moreover, the energy-dispersive X-ray spectroscopic (EDX) analyzer was used to obtain the element distribution. Before analysis, the surface of the materials was coated by spraying gold.

#### 2.2.5. Temperature programmed reduction/oxidation and $\text{H}_2$ -pulse chemisorption

Temperature programmed experiments were carried out by Autochem II 2920 apparatus to determine the reducibility nature of fresh catalysts and active metal dispersion of reduced catalysts. The sample was loaded in a U-shaped tube quartz reactor. Before the TPR measurement, the catalyst was *in-situ* degassed in inert Ar/He for 1 h at  $300^{\circ}\text{C}$  to remove any moisture and impurities, then cooled to room temperature.  $\text{H}_2$ -TPR profiles of the fresh catalysts ( $\sim 30$  mg) were recorded by increasing the temperature from  $25^{\circ}\text{C}$  to  $900^{\circ}\text{C}$  with a heating ramp of  $10^{\circ}\text{C}\cdot\text{min}^{-1}$  in the flow of 10.2%  $\text{H}_2/\text{Ar}$  (50  $\text{mL}\cdot\text{min}^{-1}$ ). Prior to  $\text{H}_2$ -pulse chemisorption test, the analysis started with a pre-reduction (*in-situ* reduction similar to the procedure applied in GSR) by heating the fresh catalysts ( $\sim 0.5$  g) from  $25^{\circ}\text{C}$  to  $700^{\circ}\text{C}$  at  $10^{\circ}\text{C}\cdot\text{min}^{-1}$  for 1.5 h under 10.2%  $\text{H}_2/\text{Ar}$  flow (50  $\text{mL}\cdot\text{min}^{-1}$ ). After cooling down to  $50^{\circ}\text{C}$  in the Ar flow, a pulse of 10.2%  $\text{H}_2/\text{Ar}$  (20  $\text{mL}\cdot\text{min}^{-1}$ ) was introduced every 4 min interval at a constant temperature until equal peaks were detected. Considering the non-homogeneity of carbonaceous species (coke) deposition on the used catalyst, an *in-situ* TPO analysis (in the GSR reactor) was performed to measure the elemental carbon via burning the coke species [25]. After 3 h GSR test, the reactor was cooled down to  $25^{\circ}\text{C}$  under Ar flow (50  $\text{mL}\cdot\text{min}^{-1}$ ). Subsequently, the temperature was raised to  $800^{\circ}\text{C}$  at a heating rate of  $10^{\circ}\text{C}\cdot\text{min}^{-1}$  under a stream of 50% Air/Ar (100  $\text{mL}\cdot\text{min}^{-1}$ , 10.5%  $\text{O}_2$ ). Temperature programmed oxidation (*in-situ* TPO) profiles were

achieved via continuously monitoring C-containing gas concentration in the reactor effluent by MicroGC (3000 A).

#### 2.2.6. Transmission electron microscopy

A transmission electron microscope (TEM, JEOL JEM-1230) with 80 kV accelerating voltage was used to observe the texture of the pre-/post-reaction catalysts as well as the type of deposited coke. The samples were prepared via dispersion catalyst powders into anhydrous ethanol solvent by sonication and then titrated onto a holey carbon-coated Cu grids, thereafter dried at ambient temperature. The Digimizer software was adopted to determine the particle size distribution and the average value of active metals on the reduced/used catalysts.

#### 2.2.7. Raman analysis

Bruker Senterra II microscope was used to analyze the nature and graphitization degree of deposited carbonaceous species on the surface of the used catalysts. Sample of approximately 30 mg was analyzed using the Raman spectrometer equipped with a 532 nm laser operating at a low laser power of 6.25 mW. The Raman spectra in the range of  $1000\text{--}2000\text{ cm}^{-1}$  were acquired based on nine points distributed among 24 nm  $\times$  24 nm square area to increase the reproducibility of the investigated material. The OPUS 7.8 software was used to measure, process, and evaluate the Raman spectra.

#### 2.2.8. X-ray photoelectron spectroscopy

To analyze the surface elemental composition and electronic states of the elements on the reduced catalysts, the X-ray photoelectron spectra (XPS) were recorded on a Perkin Elmer PHI model 5600 spectrometer equipped with a monochromatic Al-K $\alpha$  excitation source (300 W). The condition of the X-ray source worked at 1.2 kV and 10 mA under a vacuum of  $8 \times 10^{-9}$  mbar. The MultiPak 9.3.0.3 software was used to perform the spectral regions of Ni 2p, Fe 2p, Al 2p, Si 2p, and O 1s, as well as the calculation of relative atomic concentration, which were referenced by C 1s peak at 284.8 eV and quantified after curve-fitting (Gaussian-Lorentzian) and normalization of primary peaks.

#### 2.2.9. Thermogravimetric analysis

Thermogravimetric analysis (TGA) and derivative thermogravimetry (DTG) were employed to measure both the total amounts and the nature of carbonaceous species formed during the GSR reaction. In a typical test, approximately 0.5 g of used sample was loaded and heated from  $25^{\circ}\text{C}$  to  $800^{\circ}\text{C}$  with a ramping rate of  $10^{\circ}\text{C}\cdot\text{min}^{-1}$  in the presence of the air stream (100  $\text{mL}\cdot\text{min}^{-1}$ ), while the weight change as a function of temperature was recorded.

### 2.3. Catalytic tests

Glycerol steam reforming was performed in a fixed bed stainless steel reactor with a length of 40 cm and an internal diameter of 1.1 cm. The operation procedures and conditions were reported in detail in our previous work [15]. Briefly, the catalyst (0.5 g,  $< 100 \mu\text{m}$ ) was loaded into the middle reactor and then reduced in a stream of 10.2%  $\text{H}_2/\text{Ar}$  at  $700^{\circ}\text{C}$  for 1.5 h at atmospheric pressure. Pure glycerol mixed with distilled water with molar ratio of 1:9 was injected using HPLC pump at a constant flow rate of 0.057  $\text{mL}\cdot\text{min}^{-1}$  (supplied by Ar with 47  $\text{mL}\cdot\text{min}^{-1}$ ). GSR experiments using the developed catalysts were operated at  $630^{\circ}\text{C}$  for 3 h (each sample was performed at least in duplicate) and the stability test of  $\text{Ni-FA}^{\text{H}\cdot\text{Na}}$  sample was performed for 25 h in the same conditions. The gaseous products ( $\text{H}_2$ ,  $\text{CH}_4$ ,  $\text{CO}$ ,  $\text{CO}_2$ , and  $\text{C}_{2+}$ ) were analyzed on-line using a MicroGC 3000A equipped with Molecular Sieve 5A column (10 m  $\times$  320  $\mu\text{m}$   $\times$  12  $\mu\text{m}$ ) and Plot Q column (8 m  $\times$  320  $\mu\text{m}$   $\times$  30  $\mu\text{m}$ ) with Ar and He carrier gas, respectively. The condensed products were off-line qualitatively analyzed using GC (Agilent 7820A) and HPLC (SPD-M20A).

For each catalytic test, the measured concentrations for each gaseous compound were averaged over the time period of a run. The liquid by-

products and coke were analyzed and measured batch-wise at the end of each run. The catalytic activity was evaluated in terms of glycerol conversion ( $X_{GCT}$ ,  $X_{GCG}$ ,  $X_{GCL}$ , and  $X_{GCC}$ ), hydrogen yield ( $Y_{H_2}$ ), and C-containing gaseous yield ( $Y_i$ ):

- Total glycerol conversion ( $X_{GCT}$ ):
- Glycerol conversion to gaseous products ( $X_{GCG}$ ), to liquid products ( $X_{GCL}$ , excluding non-reacted glycerol), and coke ( $X_{GCC}$ ):

$$X_{GCT}(\%) = \left( 1 - \frac{\text{moles of glycerol in the outlet}}{\text{moles of glycerol in the feed}} \right) \times 100 \quad (1)$$

$$X_{GCG}(\%) = \frac{\text{moles of C atoms in the gaseous products}}{3 \times \text{moles of glycerol in the feed}} \times 100 \quad (2)$$

$$X_{GCL}(\%) = \frac{\text{moles of C atoms in the liquid products}}{3 \times \text{moles of glycerol in the feed}} \times 100 \quad (3)$$

$$X_{GCC}(\%) = \frac{\text{moles of C atoms in the coke products}}{3 \times \text{moles of glycerol in the feed}} \times 100 \quad (4)$$

$$\text{Carbon balance} = \left( 1 - \frac{\text{moles of C atoms in the outlet}}{3 \times \text{moles of glycerol in the feed}} \right) \times 100 \quad (5)$$

The number of C moles in the coke products was determined using the *in-situ* TPO analysis (integration for resulted TPO signals), as described in §2.2.5.

- Yield of  $H_2$  ( $Y_{H_2}$ ) and carbon-containing gas products ( $Y_i$ ):

$$Y_{H_2}(\%) = \frac{\text{moles of } H_2 \text{ produced}}{7 \times \text{moles of glycerol in the feed}} \times 100 \quad (6)$$

$$Y_i(\%) = \frac{n_i \times \text{moles of C in species } i}{3 \times \text{moles of glycerol in the feed}} \times 100 \quad (7)$$

$i$  stands for CO,  $CO_2$ ,  $CH_4$ , and  $C_{2+}$ , and  $n_i$  corresponds to the carbon atoms of  $i$  species.

- Average rate of sintering ( $R_s$ ) and coke/carbon species ( $R_{coke}$  and  $R_{carbon}$ ):

$$R_s = \frac{D_{Ni} \text{ in used catalyst (nm)} - D_{Ni} \text{ in reduced catalyst (nm)}}{D_{Ni} \text{ in reduced catalyst (nm)} \times \text{time on stream (h)}} \quad (8)$$

$$R_{coke} = \frac{\text{coke formed on the catalyst (mg)}}{\text{mass of catalyst (g)} \times \text{time on stream (h)}} \quad (9)$$

$$R_{carbon} = \frac{\text{elemental C existed in coke deposits (mg)}}{\text{mass of catalyst (g)} \times \text{time on stream (h)}} \quad (10)$$

Coke in the present work refers to any carbonaceous solid (covering heavy hydrocarbons and/or oxygenates [26]) deposited on the surface of used catalyst.

### 3. Results and discussion

#### 3.1. Characterization of supports and fresh catalysts

The concentration (wt%) of the major chemical components of FA and  $FA^x$  samples was measured by XRF analysis and the results are listed in Table 1. Prior to treatment, FA consisted of  $SiO_2$  (48.18%) and  $Al_2O_3$  (26.67%), followed by  $Fe_2O_3$  (13.77%), as well as less amounts of  $CaO$  (3.97%),  $K_2O$  (2.27%),  $TiO_2$  (1.68%), and  $SO_3$  (1.19%). The other metal oxides ( $MgO$ ,  $Na_2O$ ,  $P_2O_5$ , etc.) were also detected with a proportion of less than 1%. However, a variation in chemical composition was observed after FA leaching-partial-dissolution (LPD), which indicates that some components were dissolved into alkali or acid solution, especially for the FA that undergone alkali-LPD. Table 1 shows a decrease for both  $SO_3$  and  $P_2O_5$  in alkali or acid treatment, indicating that S- or P-containing species could be soluble in both solutions.  $SiO_2$  only decreases in the samples experienced alkali-LPD, as a result of the extraction of partial  $SiO_2$  by NaOH (Table S1, Eq. S1). The tendency of  $K_2O$  is similar to that of  $SiO_2$ . Moreover, the content of  $CaO$  in the samples subjected to acid-LPD is slightly lower than that of FA, which might be attributed to the dissolution of Ca-containing species into  $HNO_3$  (Table S1, Eq. S6), leading to the decrease of  $CaO$ . On the contrary, the concentration of  $Al_2O_3$  in  $FA^x$  samples is higher than that of the FA, which is attributed to the high dissolution of other components. Similar behavior is observed for  $SiO_2$  in the one-step acid-LPD sample and  $Fe_2O_3$  and  $MgO$  in the alkali-LPD samples. Moreover, the  $Na_2O$  significantly increases in  $FA^{Na}$  (4.76%) and  $FA^{H/Na}$  (7.46%), which might be attributed to the formation of Na-containing compound and/or the unwashed NaOH residue when alkali as the final step treatment (Table S1, Eqs. S1-4). In addition, the weight percentage of FA that dissolved in acid/alkali solution (DS) during the four treatments was measured and the results (Table 1) shows the following trend:  $FA^{Na/H}$  (44.3%) >  $FA^{H/Na}$  (16.9%) >  $FA^{Na}$  (10.9%) >  $FA^H$  (4.4%). It can be seen that the FA's DS in alkali-LPD was higher than that of one-step acid-LPD because the silica easily dissolved into the alkali solution. Moreover, the two-step treatment provides higher DS compared to the one-step treatment due to the dissolution of more components. The highest value acquired for  $FA^{Na/H}$  is probably because this sequence (initial alkali-LPD followed by acid-LPD) is more conducive to the dissolution of components compared to that of  $FA^{H/Na}$ .

To understand better the effect of the applied acid/alkali treatments on the behavior of components during dissolution, Fig. 1 illustrates the relative amount of oxides that remained in  $FA^x$  residues and dissolved in solution (wt%) after treatment. It can be seen that most of the phases are easily dissolved during the two-step alkali/acid-LPD, indicating that this treatment was more efficient for changing the components distribution, among the studied four treatments. The dissolution of  $SiO_2$  in one-step alkali-LPD closely resembles to that of the two-step acid/alkali routes, which is however significantly lower than that of two-step alkali/acid-LPD. Considering the negligible dissolution of  $SiO_2$  in one-step acid-LPD performance, two possible hypotheses are suggested: i) internal acid-soluble Si-containing species emerged after the initial alkali treatment or ii) novel acid-soluble Si-containing phase was formed during the initial alkali treatment (Table S1, Eq. S4) and thus further leached out in

**Table 1**  
The chemical composition and dissolution percentage of FA and  $FA^x$  supports (wt%).

supports	chemical composition (oxides, wt%) analyzed by XRF											DS <sup>a</sup>	
	$SiO_2$	$Al_2O_3$	$Fe_2O_3$	$CaO$	$K_2O$	$TiO_2$	$SO_3$	$MgO$	$Na_2O$	$P_2O_5$	$MnO$	$Cr_2O_3$	
FA	48.18	26.67	13.77	3.97	2.27	1.68	1.19	0.75	0.62	0.54	0.03	0.05	0.17
$FA^{Na}$	40.48	29.56	15.39	4.26	1.39	1.59	0.61	1.01	4.76	0.34	0.05	0.05	0.19
$FA^H$	50.38	27.56	13.64	2.68	2.25	1.41	0.02	0.78	0.63	0.29	0.05	0.06	4.4
$FA^{Na/H}$	35.70	37.74	21.32	1.01	0.70	1.88	0.16	0.94	0.12	0.15	0.03	0.05	44.3
$FA^{H/Na}$	38.53	31.72	15.71	2.78	0.91	1.40	0.03	1.03	7.46	0.10	0.02	0.03	0.17

<sup>a</sup> The weight percentage of FA that was dissolved in acid/alkali solution [DS = (mass<sub>before</sub> - mass<sub>after</sub>)/mass<sub>before</sub> × 100%].

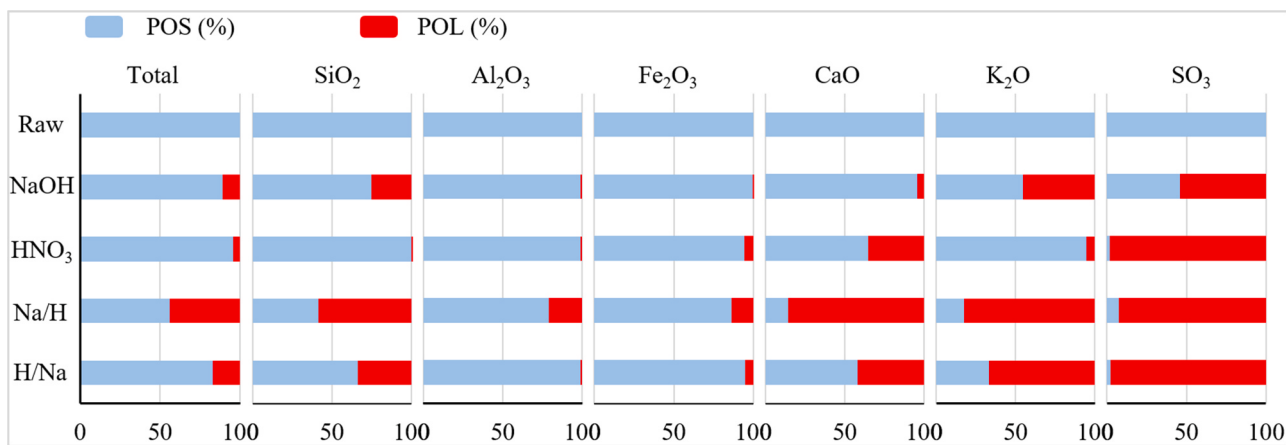


**Fig. 1.** Percentage of oxides from FA residue remained in solid phase (POS) and dissolved in liquid phase (POL) before and after the four treatments, [POS = ((1-DS)  $\times$   $W_i^x / W_i$ )  $\times$  100%, POL = (1-POS)  $\times$  100%, i refers to oxides, the values of DS,  $W_i^x$  and  $W_i$  were taken from Table 1].

following HNO<sub>3</sub> treatment (Table S1, Eq. S5). It was found that the leaching behavior of K<sub>2</sub>O is similar to that of SiO<sub>2</sub>, indicating the coexistence of the Si- and K-containing species. Moreover, the above assumptions could also be suitable to reveal the behavior of Al<sub>2</sub>O<sub>3</sub>, whose maximum dissolution appears in the two-step alkali/acid-LPD (Table S1, Eq. S4). However, its negligible dissolution in other treatments (Table S1, Eqs. S2,S8) could be attributed to i) the low amount of free Al<sub>2</sub>O<sub>3</sub>, and ii) the low solubility of Al<sub>2</sub>O<sub>3</sub> in NaOH below 160 °C [27]. In addition, similar dissolution behavior of Fe<sub>2</sub>O<sub>3</sub> and CaO is observed (Fig. 1), following the order of FA<sup>Na</sup> < FA<sup>H</sup>  $\simeq$  FA<sup>H/Na</sup> < FA<sup>Na/H</sup>. It might be argued that the Ca- and Fe-containing species within FA are more easily dissolved in acid solution (Table S1, Eqs. S6-7) rather than alkali one. Their highest dissolution was also obtained in FA<sup>Na/H</sup>, which still could be interpreted via the aforementioned plausible assumptions. Alkali-LPD as the first step could break the FA structure via dissolving Si-containing shell, providing more reaction space for subsequent acid treatment, thus leading to the removal of acid-soluble Ca- and Fe-containing species. In addition, these results illustrate that acid-soluble Ca- and Fe-containing substances not only occur on the surface of spherical FA (external), but also exist inside the FA particles (internal). Furthermore, the higher dissolution value of SO<sub>3</sub> was obtained in the FA<sup>x</sup> with acid-LPD processes (> 95%) as compared to FA<sup>Na</sup>. This demonstrates that the majority of S-containing substances were mainly present on the surface of spherical FA and could be efficiently removed using the acid solution (Table S1, Eq. S6). It should be noted that the sequence of alkali and acid has a crucial role in altering the FA chemical composition, which might further affect the catalytic activity during the steam reforming [28].

To appraise the **relationship between the FA<sup>x</sup> chemical composition and their textural change**, the detailed textural properties of designed supports and fresh catalysts (after calcination), including specific surface area (SSA), total pore volume (TPV), and average pore size (APS) are summarized in Table 2. Moreover, the corresponding N<sub>2</sub> adsorption-

desorption isotherms, consistent with type II physisorption described in the International Union of Pure and Applied Chemistry (IUPAC) classification, which matches macro-porous or non-porous materials [29], are shown in Fig. S1a-b. The H3-type hysteresis loop within the P/P° range of 0.5-1.0, recorded for all samples, is associated with the capillary condensation inside the slit-shaped pores caused by the agglomeration of grains [30,31]. Concerning the supports, FA<sup>Na/H</sup> possesses the highest BET surface area (30.22 m<sup>2</sup>•g<sup>-1</sup>), followed by FA<sup>H/Na</sup> and FA<sup>Na</sup> with 19.33 m<sup>2</sup>•g<sup>-1</sup> and 12.24 m<sup>2</sup>•g<sup>-1</sup>, respectively. Only a slight increase of SSA (1.71 m<sup>2</sup>•g<sup>-1</sup>) was obtained for FA<sup>H</sup> support as compared to that of the FA sample (1.19 m<sup>2</sup>•g<sup>-1</sup>). A similar tendency can be observed for total pore volume (Table 2). The variations of SSA and TPV for FA after four different treatments are consistent with their DS results (Table 1), indicating that the textural change of the FA<sup>x</sup> supports is intimately related to the variation of their chemical composition. It can be seen that both SSA and TPV properties could be effectively improved when alkali was applied in the activation process. This could be attributed to the fact that more Si-containing components were dissolved into alkali solution as compared to acid solution, resulting in the appearance of porous structure. The two-step treatment can achieve higher SSA and TPV than the one-step processing (Table 2), probably because more components (Si, Al, Fe, Ca, and K) within FA were leached out (Fig. 1). Moreover, the effect of the sequence of alkali/acid treatments on the FA texture was first highlighted, in which the increase of SSA and TPV for FA<sup>Na/H</sup> is higher than that of FA<sup>H/Na</sup>. This result indicates that alkali as the initial activation was more effective probably because alkali-LPD offered more contact/reaction surface for the followed acid treatment. Furthermore, the average pore sizes of the FA<sup>x</sup> supports are considerably lower than those of the FA sample (53.98 nm). This result could be attributed to the formation of minor pores during chemical treatments, confirmed by the presence of an intensified sharp peak (< 4 nm) in pore diameter distribution (insertion Fig. S1a). Besides, a broad peak ranging from 6 to 64 nm for alkali-LPD FA<sup>x</sup> samples was associated to the formation of the

**Table 2**  
Textural properties of FA, FA<sup>x</sup> supports and fresh Ni-FA, Ni-FA<sup>x</sup> catalysts.

supports	SSA <sup>a</sup> (m <sup>2</sup> •g <sup>-1</sup> )	TPV <sup>b</sup> (cm <sup>3</sup> •g <sup>-1</sup> )	APS <sup>c</sup> (nm)	fresh catalysts	SSA <sup>a</sup> (m <sup>2</sup> •g <sup>-1</sup> )	TPV <sup>b</sup> (cm <sup>3</sup> •g <sup>-1</sup> )	APS <sup>c</sup> (nm)
FA	1.19	0.02	53.98	Ni-FA	2.54	0.05	73.86
FA <sup>Na</sup>	12.24	0.14	46.67	Ni-FA <sup>Na</sup>	11.35	0.1	35.19
FA <sup>H</sup>	1.71	0.02	38.99	Ni-FA <sup>H</sup>	2.59	0.05	76.13
FA <sup>Na/H</sup>	30.22	0.27	36.31	Ni-FA <sup>Na/H</sup>	23.35	0.23	39.02
FA <sup>H/Na</sup>	19.33	0.16	32.87	Ni-FA <sup>H/Na</sup>	12.37	0.12	40.01

<sup>a</sup> specific surface area;

<sup>b</sup> total pore volume;

<sup>c</sup> average pore size.

relatively large pore after alkali treatment. These results demonstrate that  $\text{FA}^{\text{Na}/\text{H}}$ ,  $\text{FA}^{\text{H}/\text{Na}}$ , and  $\text{FA}^{\text{Na}}$  can be good candidates for catalyst support, with textures comparable to those of reported solid-waste-derived supports [32,33]. In terms of Ni incorporated catalysts (Table 2), the order of the SSA and TPV for the Ni-FA and Ni- $\text{FA}^{\text{X}}$  catalysts are consistent with those of their corresponding supports,  $\text{Ni-FA}^{\text{Na}/\text{H}} > \text{Ni-FA}^{\text{H}/\text{Na}} > \text{Ni-FA}^{\text{Na}} > \text{Ni-FA}^{\text{H}} > \text{Ni-FA}$ . It can be seen that SSA, TPV, and APS for Ni-FA and Ni- $\text{FA}^{\text{H}}$  catalysts display a slight increase relative to those of their supports. This could be attributed to the formation of new pores resulting from *i*) the arrangement/accumulation of  $\text{NiO}$  species outside of the originated pores, and/or *ii*) the nitrate redox reaction [12,20,34]. The pore size distribution (insertion Fig. S1b) clearly reveals the formation of some large pores in Ni-FA and Ni- $\text{FA}^{\text{H}}$ . However, a decrease of SSA and TPV is observed for  $\text{Ni-FA}^{\text{Na}/\text{H}}$ ,  $\text{Ni-FA}^{\text{H}/\text{Na}}$ , and  $\text{Ni-FA}^{\text{Na}}$  compared to those of the corresponding supports. This behavior could be ascribed to the blockage of the pores of their supports by  $\text{NiO}$  particles during the SSI synthesis process, and/or inevitably sintered to some degree after calcination.

The **morphological characteristics of FA and  $\text{FA}^{\text{X}}$  supports** were investigated by SEM analysis (Fig. 2). The FA owns smooth spherical morphology and non-uniform particles (diameter varying from 1 to 15  $\mu\text{m}$ ), only slit pores (gap) were found between the particles (Fig. 2a). It has been reported that pulverized coal would suffer a series of physicochemical alterations at high temperatures. The most significant feature is related to minimizing the surface energy (high surface tension), resulting in spherical FA particles, whereas their size depends on the quenching speed of the particles [35]. A similar morphology can be

observed for the  $\text{FA}^{\text{H}}$  sample (Fig. 2c), indicating that the  $\text{HNO}_3$  treatment could not destruct the spherical structure of FA. These SEM images provide evidence that FA and  $\text{FA}^{\text{H}}$  samples have a low BET surface area. However, referring to  $\text{FA}^{\text{Na}}$  (Fig. 2b),  $\text{FA}^{\text{Na}/\text{H}}$  (Fig. 2d), and  $\text{FA}^{\text{H}/\text{Na}}$  (Fig. 2e) samples, a fractured structure with a rough surface is obviously observed, rather than smooth spherical particle. This is due to the FA's main frame components ( $\text{SiO}_2$ ) dissolved into the  $\text{NaOH}$  solution, resulting in the appearance of porous structure, which is positively related to the increase in their SSA and TPV values. Moreover, the degree of breakage in terms of surface cracks and particle gaps is more apparent for the samples that received two-step treatment because more components (Si, Al, Fe, Ca, and K) were dissolved, especially for  $\text{FA}^{\text{Na}/\text{H}}$ . The SEM observations are in accordance with the results of  $\text{N}_2$  physisorption isothermal analysis. In addition, the EDX analysis was used to determine the difference in elemental composition of FA and  $\text{FA}^{\text{X}}$  supports (Fig. 2f). The elements mainly consist of O, Al, Si, Fe, Ca, Na, Mg, K, C, and Au/Pd, whereas C and Au/Pd originate from the conductive adhesive carbon tabs and coating metal, respectively. A high peak (intensity) related to Na was clearly detected in  $\text{FA}^{\text{H}/\text{Na}}$  and  $\text{FA}^{\text{Na}}$ , which is agreement with the XRF results. However, Ca is not found in  $\text{FA}^{\text{Na}/\text{H}}$ ,  $\text{FA}^{\text{H}/\text{Na}}$ , and  $\text{FA}^{\text{H}}$ , probably because of the dissolution of Ca-containing species during acid-LPD. It should be noted that some difference was observed between EDX and XRF analyses in terms of Si, Al, and Fe, due to *i*) the nonuniform particle dispersion and heterogeneous chemical composition, and *ii*) different detection mechanism (i.e. sample loading and detection limitation/depth). XRF analysis seems to more accurate for ash-type chemical composition than EDX because of the higher

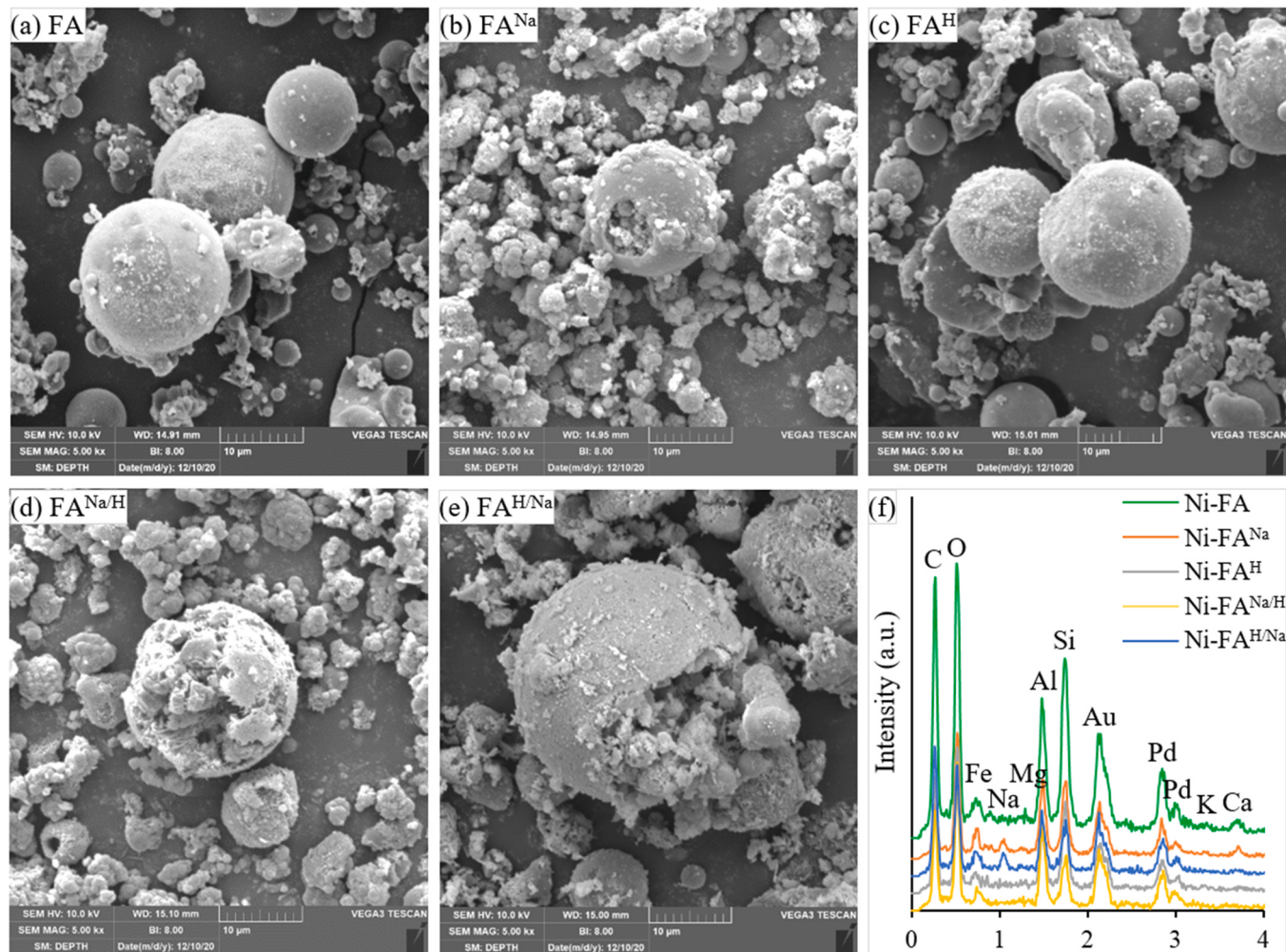


**Fig. 2.** SEM-EDX of the FA and  $\text{FA}^{\text{X}}$  supports (EDX spectroscopy from mapping analysis).

sample content and deeper detection [36].

XRD analysis were carried out to reveal **the effect of acid/alkali treatments on crystalline phases of support and catalysts**. The diffraction patterns of FA and  $\text{FA}^x$  supports are compared in Fig. 3a, where the crystalline phases of  $\text{FA}^{\text{H}}$  and  $\text{FA}^{\text{Na}}$  are similar to those of  $\text{FA}^{\text{Na}/\text{H}}$  and  $\text{FA}^{\text{H}/\text{Na}}$ , respectively. Mullite, quartz, and hematite were detected in all supports. The diffraction peaks at  $2\theta = 16.40^\circ$ ,  $25.96^\circ$ ,  $26.17^\circ$ ,  $30.92^\circ$ ,  $33.15^\circ$ ,  $35.19^\circ$ ,  $40.80^\circ$ , and  $60.55^\circ$  are assigned to the mullite phase ( $3\text{Al}_2\text{O}_3 \bullet 2\text{SiO}_2$ , ICDD file 96-710-5576). Mullite belongs to aluminosilicates, which could serve as thermostable material offering a sintering resistance at high temperatures [15]. The characteristic peaks at  $2\theta$  of  $20.85^\circ$ ,  $26.62^\circ$ ,  $36.53^\circ$ ,  $39.44^\circ$ ,  $50.11^\circ$ , and  $59.93^\circ$  correspond to quartz ( $\text{SiO}_2$ , ICDD file 96-900-9667). In addition, a large diffraction area (hump in the range of  $2\theta = 17$ – $25^\circ$ ) observed in the profile of FA and  $\text{FA}^{\text{H}}$  samples can be ascribed to the presence of amorphous silica [12], but barely discernable in the remaining samples ( $\text{FA}^{\text{Na}}$ ,  $\text{FA}^{\text{Na}/\text{H}}$ , and  $\text{FA}^{\text{H}/\text{Na}}$ ). The amorphous silica could be dissolved into NaOH solution, which is in accordance with the XRF results (Table 1) and dissolution behavior (Fig. 1-2). The diffraction peaks at  $2\theta = 24.20^\circ$ ,  $33.24^\circ$ ,  $35.71^\circ$ ,  $49.58^\circ$ ,  $54.20^\circ$ ,  $62.58^\circ$ , and  $64.15^\circ$  are attributed to the high amount of hematite phase ( $\text{Fe}_2\text{O}_3$ , ICDD file 96-901-5066). It should be noted that the intensity of hematite within alkali-LPD  $\text{FA}^x$  is stronger than that of FA and  $\text{FA}^{\text{H}}$  samples, which is attributed to the higher amount of the iron oxides in the alkali-LPD  $\text{FA}^x$  supports (Table 1). However, small peaks at  $2\theta = 25.45^\circ$ ,  $31.45^\circ$ ,  $40.80^\circ$ , and  $48.71^\circ$  are attributed to the low amount of anhydrite phase ( $\text{CaSO}_4$ , ICDD file 96-900-4097) in FA, which is hardly found in  $\text{FA}^x$  due to the small amount remained after acid/alkali treatment (Fig. 1). Moreover, the reflections at  $2\theta = 13.88^\circ$ ,  $24.17^\circ$ ,  $31.36^\circ$ ,  $34.44^\circ$ ,  $37.30^\circ$ ,  $42.52^\circ$ , and  $51.67^\circ$  belong to the hydroxy sodalite ( $\text{Na}_8\text{Al}_6\text{Si}_6\text{O}_{24}(\text{OH})_2$ , ICDD file 96-900-3330). This crystallite is typically generated in silica-undersaturated and sodium-rich environment where, sporadically, sodium can be partly substituted by potassium as  $\text{Na}_x\text{K}_{8-x}\text{Al}_6\text{Si}_6\text{O}_{24}(\text{OH})_2$  [37]. Fig. 3a shows that hydroxy sodalite appears only in  $\text{FA}^{\text{Na}}$  and  $\text{FA}^{\text{H}/\text{Na}}$  samples. Its absence in the other samples indicates the appearance of a new crystalline species during the activation when the alkali-LPD is the final process (Eq. S4). No diffraction peak for hydroxy sodalite was observed in  $\text{FA}^{\text{Na}/\text{H}}$ , probably due to its dissolution in acid solution [38]. Besides, this result also evidences the increase of the dissolution of  $\text{SiO}_2$ ,  $\text{Al}_2\text{O}_3$ , and  $\text{K}_2\text{O}$  during two-step alkali/acid treatment (Fig. 1). In addition, no diffraction peak assigned to bulk  $\text{Al}_2\text{O}_3$  crystal was detected on the studied samples, which proves its negligible dissolution during the chemical treatments (except for  $\text{FA}^{\text{Na}/\text{H}}$ , Eq. S4). The XRD characteristics are consistent with the results of XRF analysis, which confirms Si, Al, Ca, Fe, Mg, Na, and O

as the main components and the variation in their composition in the  $\text{FA}^x$  samples.

After nickel incorporation into FA and  $\text{FA}^x$  (Fig. 3b), nickel oxide ( $\text{NiO}$ , ICDD file 96-101-0096) with the characteristic peaks at  $2\theta = 37.23^\circ$ ,  $43.25^\circ$ ,  $62.83^\circ$ ,  $75.35^\circ$ , and  $79.34^\circ$ , is the new phase detected. The crystalline phases present within the supports are also identified inside the Ni- $\text{FA}^x$  catalysts. Although the same amount of Ni was loaded in all samples (7.5 wt%), chunky peaks of nickel oxide were found in the alkali-LPD samples ( $\text{Ni-FA}^{\text{Na}}$ ,  $\text{Ni-FA}^{\text{Na}/\text{H}}$ , and  $\text{Ni-FA}^{\text{H}/\text{Na}}$ ), while sharp peaks appear at the same position in Ni-FA and Ni- $\text{FA}^{\text{H}}$  (Fig. S2). Considering the high proportion of  $\text{Fe}_2\text{O}_3$  within the alkali-LPD samples,  $\text{NiO}$  could partially react with hematite to generate disordered metastable mixed oxide  $\text{Ni}_x\text{Fe}_{1-x}\text{O}$  solid solution [39,40]. In addition, the reflections of hydroxy sodalite at  $2\theta = 13.88^\circ$  and  $24.17^\circ$  became less pronounced after Ni incorporation, probably due to its decomposition during the calcination process ( $> 450^\circ\text{C}$ ) [41].

H<sub>2</sub>-TPR analysis was used to investigate **the reducibility of supports and fresh catalysts**, and the results are presented in Fig. 4. In the TPR files of FA and  $\text{FA}^x$  supports (Fig. 4a), a broad peak with high intensity of H<sub>2</sub> consumption is observed in the range of 350–700 °C, which was ascribed to the reduction of iron-containing oxides species ( $\text{Fe}_x\text{O}_y \rightarrow \text{Fe}^\circ$ ) [42]. According to the XRD results (Fig. 3a), the reducible species in the above temperature range could be attributed to the presence of hematite ( $\text{Fe}_2\text{O}_3$ ). However, the amount of H<sub>2</sub> consumption measured in TPR profiles is almost 45% less than the stoichiometric value, based on the assumption of all measured iron existed in  $\text{Fe}^{3+}$  form. Thus, except for hematite, a certain amount of low valence iron ion may exist in the aluminosilicates. Indeed, the diffraction peaks assigned to the aluminosilicates phase (mullite) in the XRD profiles of supports and catalysts (Fig. 3) can also be attributed to the incorporated iron [15]. Moreover, another peak observed in the FA sample at 860 °C could be related to the reduction of anhydrite phase ( $\text{CaSO}_4 \rightarrow \text{CaS}$ ) [17], which was not found in  $\text{FA}^x$  samples probably because of its removal during the investigated treatments.

Fig. 4b shows the TPR profiles of fresh Ni-FA and Ni- $\text{FA}^x$  catalysts. A large H<sub>2</sub> consumption peak at 495 °C was detected for all samples, attributed to the reduction of iron oxides ( $\text{Fe}_x\text{O}_y \rightarrow \text{Fe}^\circ$ ), based on the TPR analysis result of FA and  $\text{FA}^x$ . The reduction temperature of iron-containing species inside fresh catalysts shifted to a lower temperature of 495 °C in comparison with the corresponding supports (515 °C). It means that the reduction behavior of iron-containing oxides was facilitated after Ni loading, which might be associated with the H<sub>2</sub> spillover in the presence of Ni [43,44]. This implies that the dissociation of H<sub>2</sub> into atoms on the metal Ni sites can easily spillover to the surrounding iron oxides regions and thus lead to the easier reduction of iron oxides.

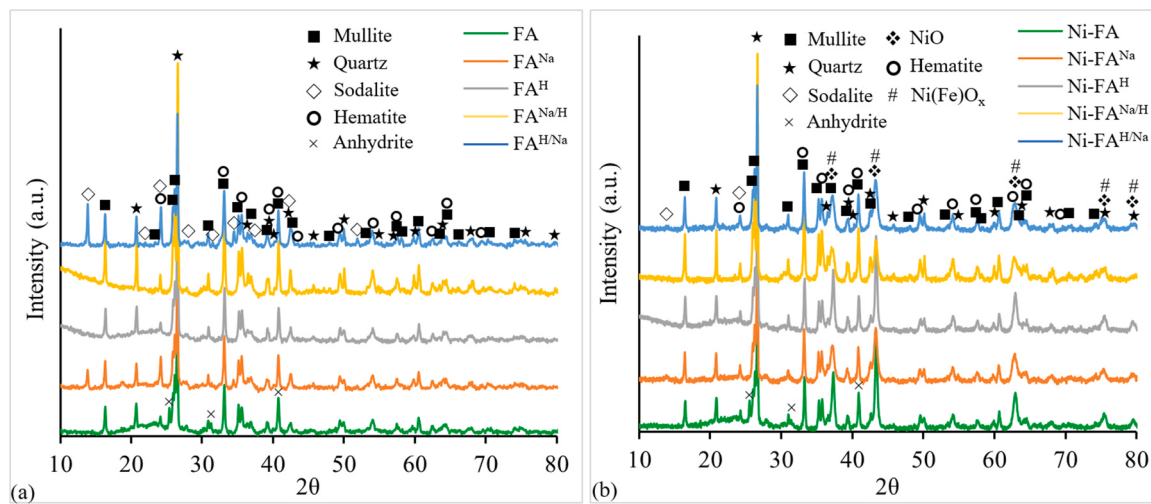


**Fig. 3.** XRD patterns of the FA,  $\text{FA}^x$  supports, and fresh Ni-FA, Ni- $\text{FA}^x$  catalysts.

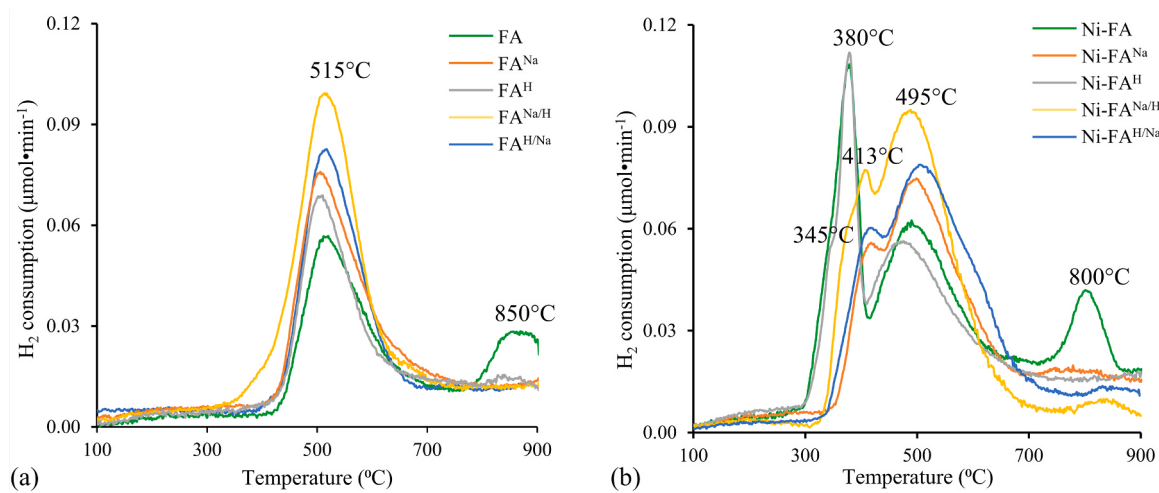


**Fig. 4.** The TPR profiles of (a) FA, FA<sup>x</sup> supports and (b) fresh Ni-FA, Ni-FA<sup>x</sup> catalysts.

In addition, a relatively narrow peak at 380 °C coupled with a shoulder peak at 345 °C for both Ni-FA and Ni-FA<sup>H</sup> samples can be assigned to the reduction of free NiO and/or NiO weakly interacted aluminosilicates on the surface of the FA particles [21]. However, in the samples undergoing alkali-LPD, the NiO reduction peak shifted to higher temperatures (around 413 °C), which could be attributed to the reduction of the Ni<sub>x</sub>Fe<sub>1-x</sub>O solid solution, indicating a medium interaction of NiO species with the iron oxides. This is consistent with the XRD analysis (Fig. 3b). In accordance with the H<sub>2</sub>-consumption of TPR analysis (Table 3), it can be concluded that the nickel oxides were completely reduced in the synthesized Ni-FA and Ni-FA<sup>x</sup> catalysts. These results suggest that 700 °C is sufficient for the catalyst pre-reduction. In addition, the reducible temperature of anhydrite (CaSO<sub>4</sub>) shifts to a lower value in the fresh Ni-FA catalyst, as also reported by Lu et al. [45].

### 3.2. Characterization of reduced catalysts

Metallic particles are known as active centers for reforming reaction, whose characteristics are crucial, including crystalline formula, particle size/distribution, and active sites dispersion. To reveal the relationship between catalytic activity and the formed active sites after reduction, the characterizations (XRD, XPS, TEM, SEM-EDX, and H<sub>2</sub>-pulse chemisorption) of the reduced Ni-FA and Ni-FA<sup>x</sup> catalysts are indispensable. Prior to the characterization analyses, the fresh Ni-FA and Ni-FA<sup>x</sup>

catalysts were activated by a reduction pretreatment under H<sub>2</sub> flow at 700 °C for 1.5 h (the same reduction conditions before GSR reaction). The textural properties of the reduced Ni-FA and Ni-FA<sup>x</sup> catalysts are shown in Table 4. Compared to fresh catalysts (Table 2), only a slight change in terms of specific surface area and total pore volume was found for the reduced Ni-FA and Ni-FA<sup>x</sup> catalysts, except for Ni-FA<sup>Na/H</sup>. This is probably related to the evaporation of H<sub>2</sub>O leading to the change of the pore structure (Fig. S1c), and/or the change of crystalline size due to the nickel/iron oxides reduction. On the contrary, the SSA of Ni-FA<sup>Na/H</sup> obviously decrease after reduction (from 23.35 to 16.67 m<sup>2</sup>·g<sup>-1</sup>), which could be attributed to *i*) enlargement of pores due to the existence of fragile skeleton (resulted by the severe chemical components outflow), and/or *ii*) blockage of micropores by the nickel species deposited on FA surface (Fig. S1c) [46].

Compared to XRD patterns of fresh catalysts (Fig. 3), mullite, quartz, and anhydrite are still visible in the reduced Ni-FA and Ni-FA<sup>x</sup> catalysts (Fig. 5a). The new diffraction lines appeared at 2θ = 44.61°, 51.93°, and 76.51° belong to crystalline phases of metallic Fe (ICDD file 96-901-6481). The new peaks at 2θ = 44.41°, 51.75°, and 76.23° appeared in XRD patterns of Ni-FA and Ni-FA<sup>H</sup> are attributed to crystalline phases of metallic Ni (ICDD file 96-901-2973). No peak related to the nickel oxides and iron oxides was noticed. These results are in agreement with the TPR analysis results (Fig. 4 and Table 3), confirming that nickel and iron species in fresh catalysts are entirely reduced under the reduction

**Table 3**  
Reduction behavior of the supports and fresh catalysts in H<sub>2</sub>-TPR analysis.

chemical treatment	molar content (mmol·g <sup>-1</sup> ) <sup>a</sup>			H <sub>2</sub> consumption in TPR (mmol·g <sup>-1</sup> ) <sup>b</sup>			molar ratio H <sub>2</sub> /Fe (%) <sup>c</sup>	H <sub>2</sub> consumption in TPR (mmol·g <sup>-1</sup> ) <sup>d</sup>			reduction degree (%) <sup>e</sup>
	support		catalyst	support		catalyst		support		catalyst	
	Fe	Fe	Ni	Fe	Fe	Ni		Fe	Fe	Ni	
-	1.73	1.55	1.24	1.22		2.33	70.5	1.10	1.23		99.2
NaOH	1.93	1.74	1.25	1.48		2.59	76.7	1.33	1.26		100
HNO <sub>3</sub>	1.71	1.53	1.24	1.41		2.52	82.5	1.26	1.26		100
NaOH/HNO <sub>3</sub>	2.67	2.41	1.25	2.82		3.79	106	2.55	1.24		99.2
HNO <sub>3</sub> /NaOH	1.97	1.77	1.25	1.56		2.66	79.2	1.41	1.25		100

<sup>a</sup> The concentration of the elements are measured by XRF analysis.

<sup>b</sup> H<sub>2</sub> consumption obtained from TPR profiles below 700 °C (the reduction temperature considered before GSR).

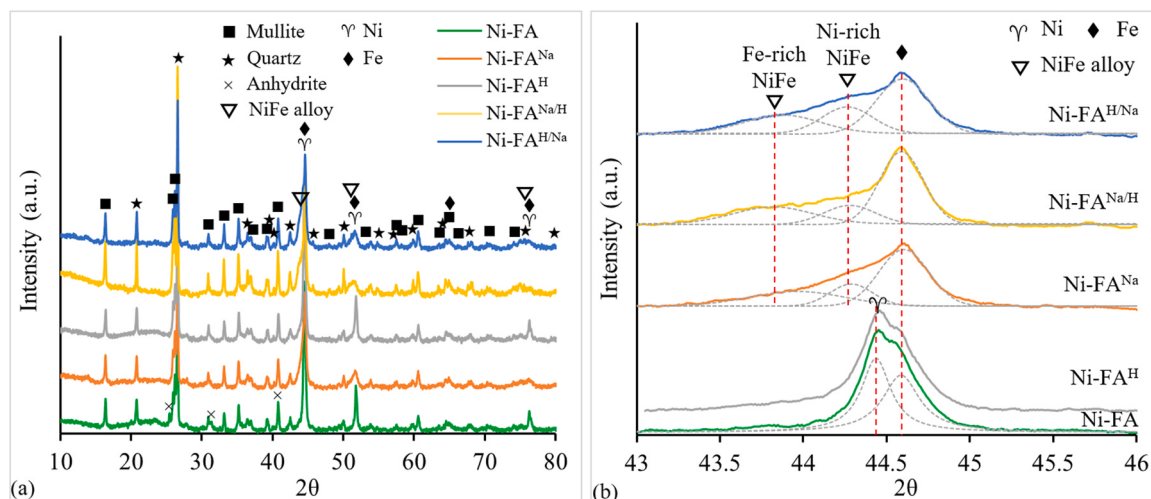
<sup>c</sup> Molar ratio of H<sub>2</sub> to Fe = (H<sub>2</sub> consumption in TPR for support) / (molar content of iron in support).

<sup>d</sup> H<sub>2</sub> consumption of Fe and Ni in catalyst was calculated based on the same molar ratio of H<sub>2</sub>/Fe in supports.

<sup>e</sup> Reduction degree of Ni = (H<sub>2</sub> consumption of Ni in TPR) / (the stoichiometry H<sub>2</sub> consumption of the Ni).

**Table 4**Textural features of reduced Ni-FA and Ni-FA<sup>x</sup> and the crystal size of metallic species.

samples	SSA <sup>a</sup> (m <sup>2</sup> •g <sup>-1</sup> )	TPV <sup>b</sup> (cm <sup>3</sup> •g <sup>-1</sup> )	APS <sup>c</sup> (nm)	Ni <sup>o</sup> (nm)	Ni-rich NiFe alloy (nm)	Fe-rich NiFe alloy (nm)	Fe <sup>o</sup> (nm)
Ni-FA	2.42	0.04	63.01	42.2	—	—	32.9
Ni-FA <sup>Na</sup>	12.11	0.13	40.70	—	29.0	12.8	25.0
Ni-FA <sup>H</sup>	2.69	0.05	48.84	38.3	—	—	30.4
Ni-FA <sup>Na/H</sup>	16.67	0.20	47.07	—	23.8	15.5	29.0
Ni-FA <sup>H/Na</sup>	12.73	0.13	43.97	—	25.2	15.1	23.2

<sup>a</sup> specific surface area;<sup>b</sup> total pore volume;<sup>c</sup> average pore size.Fig. 5. XRD patterns of the reduced Ni-FA and Ni-FA<sup>x</sup> catalysts.

conditions (700 °C, 1.5 h). Note that the peak in the range of 43–45° is amplified and deconvoluted due to the peaks overlap of metallic Ni and Fe (Fig. 5b). The left tail broad peaks appeared in Ni-FA<sup>Na</sup>, Ni-FA<sup>Na/H</sup>, and Ni-FA<sup>H/Na</sup> covers metallic Ni, Fe, and NiFe alloy. The formation of NiFe alloys was attributed to the exposure of iron due to the broken FA spherical particles after alkali-LPD. Because of the difference in the ionic radius of Fe and Ni, the lattice is distorted and a small shift in the peak position was therefore observed [47]. The peak of alloy shifts slightly to the low position but is closer to the pure metallic Ni diffraction, which could indicate the Fe consolidation in the Ni lattice [48]. Combined with the results of H<sub>2</sub>-TPR, the Gaussian-type deconvoluted diffraction lines presented at 43.83° and 44.26° are attributed to the Fe-rich and Ni-rich NiFe alloys (ICDD file 00-012-0736 and 00-038-0419), respectively, which originated from the reduction of the Ni<sub>x</sub>Fe<sub>1-x</sub>O solid solution [49, 50]. This result also provides a proof for the high reduction temperature related to nickel oxides species (413 °C) in fresh Ni-FA<sup>Na</sup>, Ni-FA<sup>Na/H</sup>, and Ni-FA<sup>H/Na</sup> catalysts (Fig. 4b). Furthermore, the average crystal size of metallic Ni, Fe, and NiFe alloys in these reduced catalysts was estimated by Scherrer analysis after Rietveld refinement (Table 4). The crystal size of monometallic Ni and bimetallic NiFe vary in the range of 42.2–43.3 nm and 23.8–29 nm (12.8–15.5 nm for Fe-rich NiFe alloy), respectively. Obviously, the particle size corresponding to NiFe alloys is smaller than that of Ni<sup>o</sup> because iron breaks the integrity of surface nickel ensembles [51]. Furthermore, the NiFe alloys could stabilize Ni particles and decrease their surface mobility, protecting against particle agglomeration, as will be further discussed through TEM and H<sub>2</sub>-pulse chemisorption analysis.

XPS analysis was performed to investigate the surface elemental composition (and their valence states) of reduced Ni-FA and Ni-FA<sup>x</sup> catalysts. The survey spectrum of core level XPS confirms the existence of O, Si, Al, Ca, Ni, Fe, Na, Mg, K, and Ti elements on the surface of

reduced catalysts (Fig. S3), which is in line with the XRF results (Table 1). C 1s peak was set to 284.8 eV to calibrate the other elements, and the quantitatively analyzed data (atom %) obtained from XPS-peak-differentiating-imitating were presented in Fig. S3. The atomic ratio of Si/Al in the Ni-FA and Ni-FA<sup>H</sup> samples is higher than that of Ni-FA<sup>Na</sup>, Ni-FA<sup>Na/H</sup>, and Ni-FA<sup>H/Na</sup>, indicating that part of Al-O-Si structure was broken due to the extraction of Si-containing species by alkali solution. Fig. 6 shows the high-resolution XPS spectra of Ni-FA and Ni-FA<sup>x</sup> catalysts for Ni 2p and Fe 2p regions, and the corresponding binding energies are listed in Table 5.

The spin-orbital peaks of Ni 2p as well as their consecutive shake-up satellite lines are found at 851–865 eV (sat. 858–860 eV) and 870–880 eV (sat. 876–878 eV), which are attributed to the Ni 2p<sub>3/2</sub> and Ni 2p<sub>1/2</sub>, respectively. Ni<sup>o</sup> species is generally considered to have a large difference with Ni<sup>2+</sup> species (~ 3 eV) as already reported in the literature [15]. Thus, the Ni 2p<sub>3/2</sub> peaks located around 851.8–852.3 eV and 855.4 eV binding energies could be assigned to Ni<sup>o</sup> and Ni<sup>2+</sup> species, respectively. From Table 3, it can be seen that a complete reduction is achieved for NiO under the present reduction condition. Thus, the existence of Ni<sup>2+</sup> on the surface of reduced catalysts could stem from the surface re-oxidation of metallic Ni nanoparticles upon exposure to the atmosphere [46]. Moreover, the differences of Ni 2p<sub>3/2</sub> spectra between the Ni-FA and Ni-FA<sup>x</sup> catalysts are observed (Fig. 6a). The binding energy of Ni<sup>o</sup> on the surface of alkali-LPD FA<sup>x</sup> supports was slightly shifted (~ 0.5 eV) to lower values in comparison to those of Ni-FA and Ni-FA<sup>H</sup>. This may happen as a cause of intimate interaction of Ni and Fe, resulting in the formation of NiFe alloys (Fig. 5b), which affects the electronic environment of nickel species, (i.e., the charge transfer from Fe to Ni) [44]. The binding energies at ~711 eV and ~705 eV in the high-resolution XPS spectra of Ni-FA and Ni-FA<sup>x</sup> catalysts in Fe 2p region (Fig. 6b) can be assigned to Fe<sup>3+</sup> and Fe<sup>o</sup>, respectively. Fe<sup>3+</sup> could arise

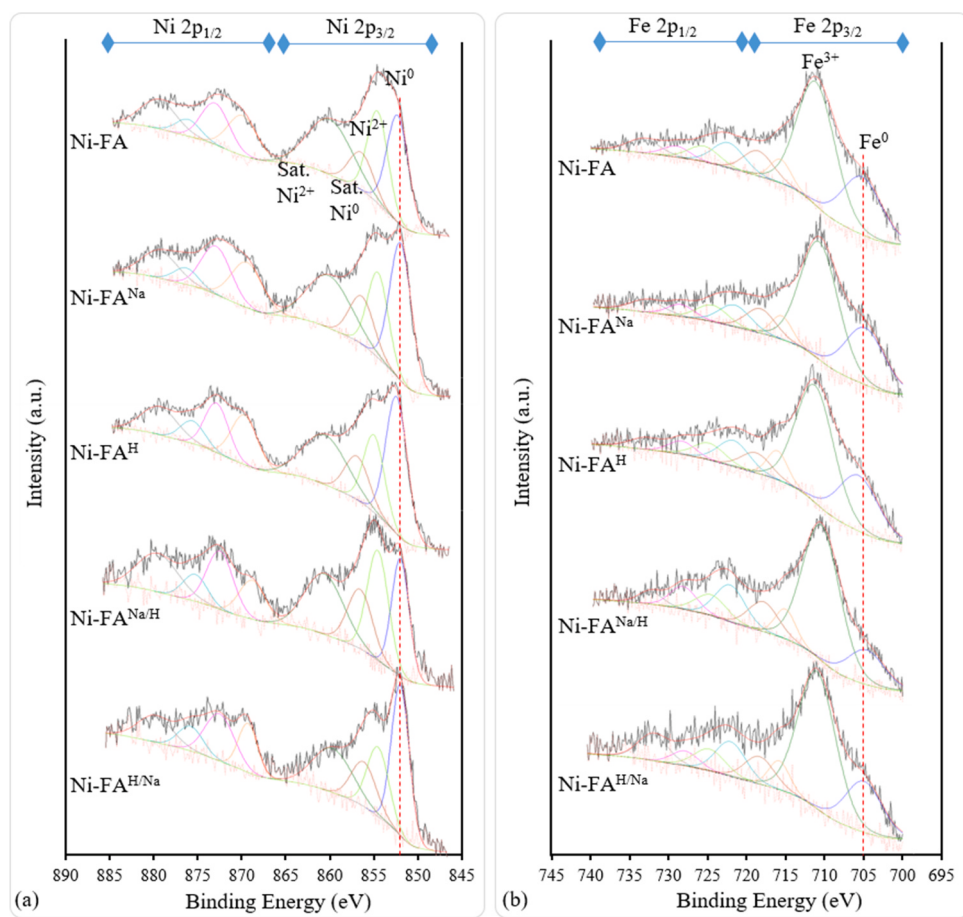


**Fig. 6.** High-resolution XPS spectrum of reduced Ni-FA and Ni-FA<sup>x</sup> catalysts; (a) Ni 2p, (b) Fe 2p regions.

**Table 5**

XPS binding energies (eV) and surface elemental composition of reduced Ni-FA and Ni-FA<sup>x</sup> catalysts.

sample	Ni 2p <sub>3/2</sub>		Ni 2p <sub>3/2</sub> sat.		Fe 2p <sub>3/2</sub>		O 1s			Si 2p		Al 2p	
	Ni <sup>0</sup>	Ni <sup>2+</sup>	Ni <sup>0</sup>	Ni <sup>2+</sup>	Fe <sup>0</sup>	Fe <sup>3+</sup>	O-M <sup>a</sup>	Si-O-Al	Si-O-Si	Si-O-Al	Si-O-Si	[AlO <sub>4</sub> ]	[AlO <sub>6</sub> ]
Ni-FA	852.2	854.4	856.3	859.9	705.2	711.0	529.9	531.5	532.7	101.9	103.0	73.9	75.0
Ni-FA <sup>Na</sup>	851.8	854.4	856.3	860.0	704.9	710.8	529.8	531.1	532.4	101.8	102.9	74.0	75.0
Ni-FA <sup>H</sup>	852.3	854.5	856.8	860.5	705.6	711.2	530.0	531.8	533.4	101.8	102.8	74.1	75.1
Ni-FA <sup>Na/H</sup>	851.8	854.4	856.4	860.5	704.7	710.5	529.8	531.1	532.5	102.0	103.2	74.0	75.0
Ni-FA <sup>H/Na</sup>	851.8	854.4	856.0	859.5	704.9	711.0	529.8	531.3	532.6	101.9	103.0	74.0	75.0

<sup>a</sup> O-M derived from metal oxides (Fe, Ni, Ca etc.).

from the impurity (Fe<sub>2</sub>O<sub>3</sub>) derived from atmospheric reoxidation contamination. It was found that the charge transfer effect also leads to the shift of metallic Fe binding energies (~ 0.5 eV) to lower values in alkali-LPD samples.

In addition to Ni 2p and Fe 2p spectrums, the deconvoluted peaks in Al 2p, Si 2p, and O 1s regions are presented in Fig. S4. It is clear that their binding energies are consistent for all reduced catalysts. For Al 2p, XPS can differentiate between tetrahedral aluminum [AlO<sub>4</sub>] and octahedral aluminum [AlO<sub>6</sub>] in the range of 72–77 eV (Fig. S4a) [34]. [AlO<sub>4</sub>] and [AlO<sub>6</sub>] mainly originate from the mullite crystalline structure, as confirmed by XRD analysis. The binding energy of former Al (at 74 ± 0.1 eV) is generally lower than that of latter Al (at 75 ± 0.1 eV). The XPS spectra in Si 2p region was also deconvoluted into two different peaks at ~102 eV and ~103 eV binding energies (Fig. S4b), which can be assigned to the non-bridging silicon (Si-O) and bridging silicon (Si-O-Si), respectively [52]. The bridging silicon is mainly derived from quartz and mullite phases, whereas the non-bridging is mostly originated from aluminosilicates. A relatively wide O 1s spectrum ranging

from 527 to 535 eV binding energy could be deconvoluted into three different lattice oxides (Fig. S4c) based on XRD results. The first deconvoluted peak at ~533 eV is assigned to oxygen atoms in Si-O-Si bonds, another one centered at ~531 eV to the Si-O-Al bonds, and the signal at ~530 eV to O-(Ni, Fe, Ca, etc.) bonds. These results show that the acid/alkali treatments mainly affect the amount of Al, Si, and O (the intensity of XPS peaks) rather than their valence states (the binding energies of the corresponding XPS peaks), in contrast to Ni and Fe active metals.

In addition, TEM analysis was applied to investigate the morphology and size distribution of metallic particles (Ni and NiFe alloy exist as dark points in TEM images) on the surface of the reduced catalysts. As seen in Fig. 7, the dispersion of metallic particles was significantly affected by the selected treatment approaches resulted from the changed composition and structure of FA support. The agglomeration of polygon-shape Ni particles could be observed on the surface of the Ni-FA and Ni-FA<sup>H</sup> samples (Fig. 7a,c), due to the weak interaction between Ni and support. According to the size distribution histograms displayed in Fig. 7, Ni-FA

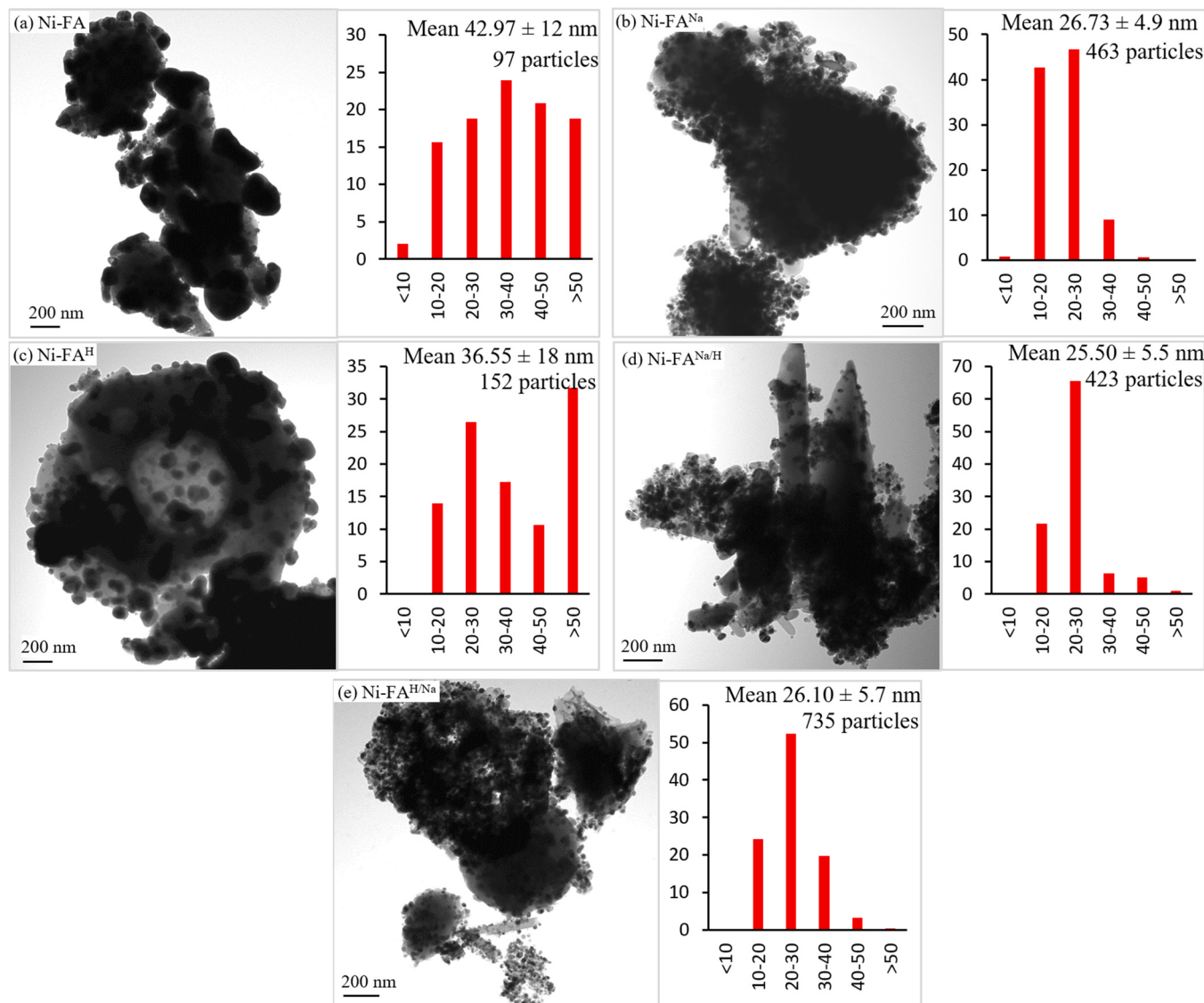


**Fig. 7.** TEM morphological characterizations and metallic particle size distributions of the reduced catalysts; (a) Ni-FA, (b) Ni-FA<sup>Na</sup>, (c) Ni-FA<sup>H</sup>, (d) Ni-FA<sup>Na/H</sup>, and (e) Ni-FA<sup>H/Na</sup>.

and Ni-FA<sup>H</sup> exhibit a wide particle size distribution with an average Ni size of 42.97 and 36.55 nm, respectively. The results for Ni-FA<sup>Na</sup>, Ni-FA<sup>Na/H</sup>, and Ni-FA<sup>H/Na</sup> are significantly different from Ni-FA and Ni-FA<sup>H</sup>. Ni supported on alkali-LPD FA<sup>x</sup> catalysts have a higher dispersion of metallic particles with smaller average diameter of ca. 26 nm along with a rather narrow size distribution (Fig. 7b,d,e). These results could be attributed to *i*) the high specific surface area of alkali-LPD FA<sup>x</sup> supports (Table 4), which could provide more space for a higher particle dispersion along with smaller particle size and *ii*) the formation of the NiFe alloys within the alkali-LPD Ni-FA<sup>x</sup> catalysts (Fig. 5), which limit the migration of metallic particles resulting in a good dispersion coupled with smaller particle size. The particle size values estimated by TEM are consistent with those obtained by XRD analysis via the Scherrer equation. In addition, the EDX elemental mapping analysis (Fig. S5) also reveals a wider distribution of the major elements (Ni, Fe, Si, and Al) over Ni-FA<sup>Na</sup>, Ni-FA<sup>Na/H</sup>, and Ni-FA<sup>H/Na</sup> catalysts as compared to Ni-FA and Ni-FA<sup>H</sup>, which is in line with the TEM results.

To obtain quantitative information on the capacity and dispersion of metallic active sites, H<sub>2</sub>-pulse chemisorption analysis was performed for the reduced Ni-FA and Ni-FA<sup>x</sup> catalysts (Table 6). Higher H<sub>2</sub> chemisorption and consequently Ni<sup>o</sup> dispersion are obtained on alkali-LPD

supports compared to the other catalysts: Ni-FA<sup>H/Na</sup> (1.45‰) > Ni-FA<sup>Na</sup> (1.21‰) > Ni-FA<sup>Na/H</sup> (0.6‰) > Ni-FA<sup>H</sup> (0.37‰) > Ni-FA (0.06‰). This could be attributed to the higher surface area and porosity of the FA<sup>x</sup> support treated by alkali-LPD, providing more space for Ni loading than that of the FA<sup>H</sup> and FA supports (Table 2). In addition, the formation of NiFe alloys in alkali-LPD catalysts could also be beneficial for the well-dispersion of Ni since the formation of NiFe alloys limits the spontaneous transmission of Ni<sup>o</sup> due to the strong interaction. By contrast, the lower value of metal active sites obtained for Ni-FA and Ni-FA<sup>H</sup> catalysts could be attributed to Ni agglomeration because of their limited surface area and weak interaction between Ni and support. These results are consistent with the TEM observation (Fig. 7). However, the dispersion of metallic active sites estimated based on the particle size ( $d_M$ , nm) from TEM results (Table 6) is significantly higher than that obtained by H<sub>2</sub>-pulse chemisorption. The difference in the dispersion between H<sub>2</sub> adsorption and TEM could be explained by the suppression of H<sub>2</sub> adsorption due to the presence of Fe [49]. Especially for the Ni-FA<sup>Na/H</sup> catalyst with the highest Fe content (14.61 wt%), the proportion of chemical elements within FA could be considerably adjusted by alkali solution treatment. A similar behavior has been reported in the literature [49,53]. Therefore, a certain amount of Fe inside FA would

**Table 6**H<sub>2</sub>-pulse chemisorption results of the reduced Ni-FA and Ni-FA<sup>x</sup> catalysts.

samples	content (mmol·g <sup>-1</sup> <sub>catalyst</sub> ) <sup>a</sup>		H <sub>2</sub> adsorption (μmol·g <sup>-1</sup> <sub>catalyst</sub> ) <sup>b</sup>	metal dispersion (%)
	Ni	Fe	H <sub>2</sub> adsorption <sup>c</sup>	TEM <sup>d</sup>
Ni-FA	1.32	1.64	0.09	0.006
Ni-FA <sup>Na</sup>	1.33	1.85	1.92	0.121
Ni-FA <sup>H</sup>	1.31	1.62	0.54	0.037
Ni-FA <sup>Na/H</sup>	1.36	2.62	1.20	0.060
Ni-FA <sup>H/Na</sup>	1.33	1.89	2.33	0.145

<sup>a</sup> The moles of the elements in reduced Ni-FA and Ni-FA<sup>x</sup> catalysts, measured by XRF.

<sup>b</sup> Data were obtained from H<sub>2</sub>-pulse chemisorption analysis for the reduced Ni-FA and Ni-FA<sup>x</sup> catalysts.

<sup>c</sup> Metal dispersion = 2 × H<sub>2</sub> adsorption/amount of reduced (Ni + Fe), taking a reduction degree of 100% for Ni and Fe into consideration according to the TPR profiles (Fig. 4) and XRD profiles (Fig. 5) below 700 °C (the reduction pre-treatment temperature considered before pulse chemisorption analysis).

<sup>d</sup> Metal dispersion by TEM, the dispersion of Ni-FA and Ni-FA<sup>H</sup> can be calculated as A<sub>Ni</sub>/d<sub>M</sub> (nm); the dispersion of Ni-FA<sup>Na</sup>, Ni-FA<sup>Na/H</sup>, and Ni-FA<sup>H/Na</sup>, Ni and Fe contents (wt%) are taken into account as follows ((A<sub>Ni</sub> × Ni) / (Ni + Fe) + (A<sub>Fe</sub> × Fe) / (Ni + Fe))/d<sub>M</sub> (nm), A<sub>Ni</sub> = 0.971 [54], A<sub>Fe</sub> = 1.225 [55], d<sub>M</sub> was the metallic particle size obtained from TEM (Fig. 7).

enhance the metal-support interaction and Ni dispersion via the formation of Ni-rich NiFe alloy (Ni-FA<sup>H/Na</sup> and Ni-FA<sup>Na</sup>). However, an excess of Fe would shield the Ni active surface area as a result of the formation of more Fe-rich NiFe alloy, which would affect their catalytic active behavior during SR process [49].

### 3.3. Catalytic performance for GSR process

The catalytic performance of the reduced Ni-FA and Ni-FA<sup>x</sup> catalysts for GSR process was first investigated at 630 °C, S/C = 3, and WHSV = 7.37 h<sup>-1</sup> for TOS = 3 h time on stream (TOS), based on the thermodynamic analysis [15]. To assess the extent of pyrolysis reaction and the catalytic activity of Fe inside the supports, which can accompany the GSR process, blank and support (non-nickel) tests were also performed at the same reforming conditions, respectively. Fig. 8 illustrates the total glycerol conversion (X<sub>GCT</sub>, Eq. 1), glycerol conversion to gases (X<sub>GCG</sub>, Eq. 2), to liquids (X<sub>GCL</sub>, Eq. 3), and to carbon (X<sub>GCC</sub>, Eq. 4), hydrogen yield (Y<sub>H2</sub>, Eq. 7), C-containing gaseous yield (Y<sub>i</sub>, Eq. 7), as well as the molar ratio of H<sub>2</sub>/CO and CO<sub>2</sub>/CO. The C-containing gaseous products [CO<sub>2</sub>, CO, CH<sub>4</sub>, and C<sub>2+</sub> (ethylene and ethane)] were detected for all samples. The liquid products detected in the condensed phase are mainly acetaldehyde, methanol, acetone, acrolein, glycolaldehyde, dihydroxyacetone, allyl alcohol, glyceraldehyde, acetic acid, and hydroxyacetone (Table S2). A carbon balance error of less than 4% was obtained (Eq. 5) for GSR test, which might be accredited to the undetected liquid products in the condensate phase and/or their evaporation during

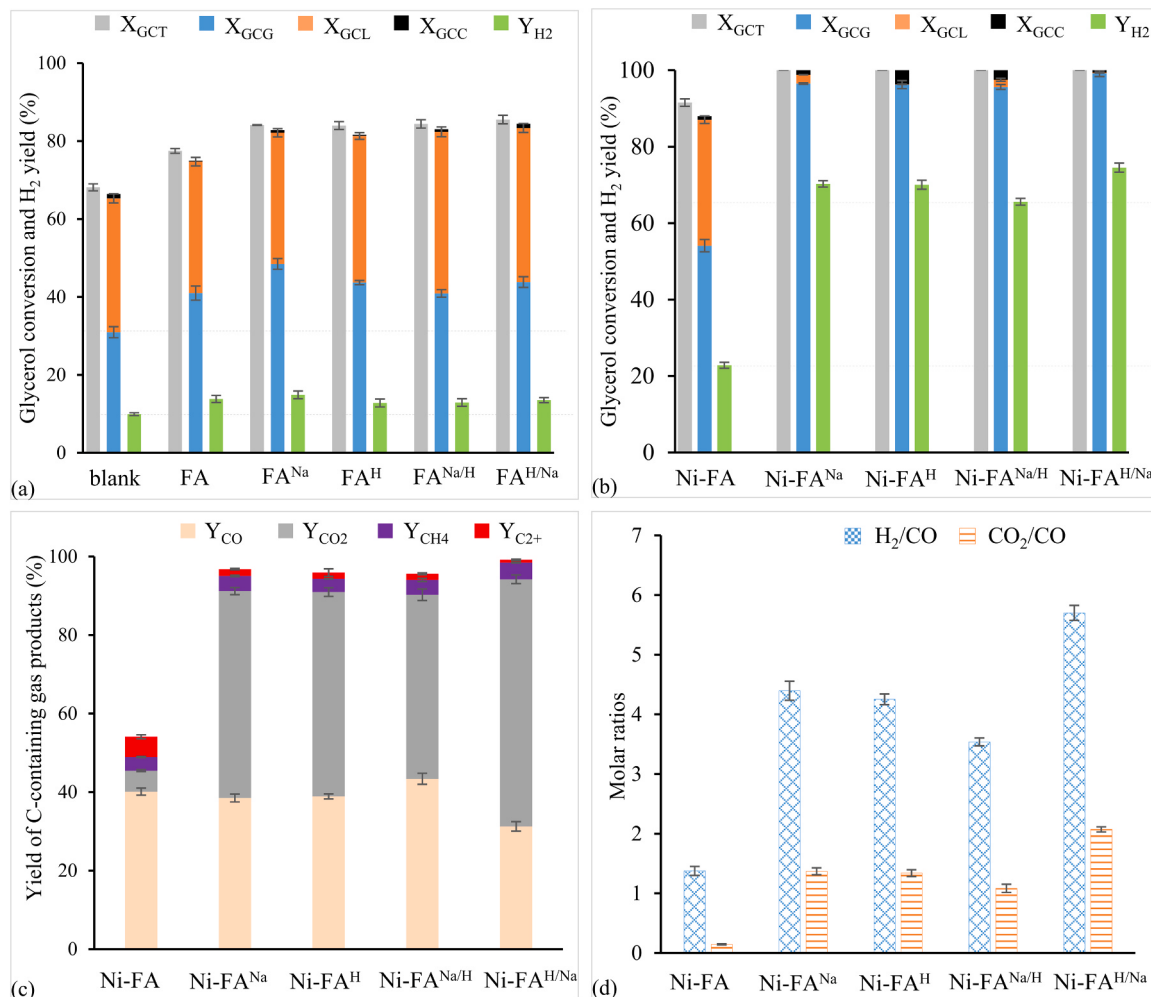


**Fig. 8.** The GSR performance over the FA, FA<sup>x</sup> supports and Ni-FA, Ni-FA<sup>x</sup> catalysts. The results for the blank test are also presented in (a) for the sake of comparison. [Reaction conditions: T = 630 °C, P = 1 atm, WHSV = 7.37 h<sup>-1</sup>, S/C = 3; TOS = 3 h].

transmission [15,56].

For the samples without nickel (Fig. 8a), glycerol significantly decomposes with  $X_{GCT}$  of 68.1–85.5%, while the  $X_{GCG}$  is only 30.9–48.5% along with a high  $X_{GCL}$  (33.7–41.5%), consequently producing low  $Y_{H2}$  (9.9–14.9%). In addition, the  $X_{GCG}$  and  $Y_{H2}$  of the FA and  $FA^x$  supports are slightly higher than those of the blank test. These results indicate that the bare FA and  $FA^x$  supports have low catalytic activity due to the existence of iron species beneficial for steam reforming [57]. The Ni incorporated catalysts (Fig. 8b) generate higher values for  $X_{GCT}$  (91.5–100%),  $X_{GCG}$  (54.1–99.2%), and  $Y_{H2}$  (22.8–74.5%) compared to those of the non-nickel samples. This could be attributed to the fact that Ni is more effective for the cleavage of C-C, C-H, and O-H bonds than Fe. However, the Ni-FA samples exhibit amongst the lowest catalytic activity,  $X_{GCG}$  and  $Y_{H2}$  reaching 54.1% and 22.8%, respectively. Notwithstanding the slightest Ni dispersion (Table 6), the low values of  $X_{GCG}$  and  $Y_{H2}$  corresponding to Ni-FA could be credited to the catalyst poisoning owing the presence of high sulfur content within FA (Table 1). It has been reported that sulfur is preferentially adsorbed on the surface of metallic Ni during SR leading to the deactivation of  $Ni^\circ$  active sites and consequently, inhibiting its catalytic activity in GSR [45]. This could be the cause of the inferior catalytic performance of Ni-FA [15]. By contrast, the catalytic performance of Ni- $FA^x$  was significantly improved (Fig. 8b) by removing most sulfur-containing species (Fig. 1). The highest values of  $X_{GCG}$  (99.2%) and  $Y_{H2}$  (74.5%) are obtained over the Ni- $FA^{H/Na}$ , followed by Ni- $FA^{Na}$  (96.5% and 70.3%), Ni- $FA^H$  (96.2% and 70%), and Ni- $FA^{Na/H}$  (95.6% and 65.6%). This result is in agreement with the dispersion of metallic Ni within  $FA^x$  supports (Table 6). As discussed in §3.2, Ni- $FA^{H/Na}$  owns the highest Ni dispersion among the synthesized Ni- $FA^x$  catalysts, and the Ni dispersion of Ni- $FA^x$  is higher compared to Ni-FA. However, the catalytic activity of the Ni- $FA^H$  catalysts is slightly better than that of the Ni- $FA^{Na/H}$  catalyst, although the number of metallic Ni sites for the former catalyst is slightly lower than that of the latter catalyst. This might be attributed to the rearrangement of  $Ni^\circ$  over the Ni- $FA^H$  catalyst during the GSR could increase the  $Ni^\circ$  active surface area, which was responsible for its good catalytic performance [15,58]. Besides, the excessive Fe exposure inside  $FA^{Na/H}$  was unfavorable because of the formation of more Fe-rich NiFe alloys, which decreased the active surface concentration of nickel [49]. Fig. 8b confirms that the removal of sulfur (poisonous impurity) and/or the appropriate formation of NiFe alloy are beneficial to the significant improvement of the catalytic activity of Ni- $FA^x$  catalysts. Moreover, the substantial alteration in the chemical composition of  $FA^x$  during the alkali/acid treatments (especially the proportion of elements like Si, Fe, Na, S, etc. within the FA support) leads to different catalytic performances of Ni- $FA^x$  catalysts.

Generally, the GSR process mainly involves the pyrolysis of glycerol to produce syngas (Table S3, Eq. S9), whereas  $H_2$  production is further promoted by WGS reaction (Table S3, Eq. S10) in the presence of steam. Several side reactions can occur, including CO and  $CO_2$  methanation (Table S3, Eqs. S11–12),  $CH_4$  reforming (Table S3, reverse Eqs. S11–12), and coke formation (Table S3, Eqs. S13–16). A catalyst with high activity would help to remove the adsorbed CO and resist to coke formation, thus increasing the  $H_2$  production. Therefore, the yield of C-containing gaseous species ( $CO$ ,  $CO_2$ ,  $CH_4$ , and  $C_{2+}$ ) and the molar ratio of  $H_2/CO$  and  $CO_2/CO$  are determined to evaluate the catalytic behavior of Ni-FA and Ni- $FA^x$  catalysts. As seen in Fig. 8c–d,  $Y_{CO_2}$  (5.4%) and  $H_2/CO$  ratio (1.4) in the Ni-FA sample are considerably lower compared to Ni- $FA^x$  catalysts ( $Y_{CO_2} = 46.9$ –63% and  $H_2/CO = 3.5$ –5.7), however,  $Y_{CO}$  is quite similar (31.3–43.4%). These results indicate that the catalytic selectivity to  $CO_2$  was limited in the case of Ni-FA.

To investigate the activity of Ni over the FA support for glycerol pyrolysis and WGS reactions, we compared the yield of C-containing gaseous products for Ni-FA with the corresponding FA support and the blank test (Fig. S6). After Ni addition to FA,  $Y_{CO_2}$  only shows a slight increase from 2.3% to 5.4%, while  $Y_{CO}$  increased significantly from 28.5% to 40.1%. These results indicate that the WGS reaction over the

Ni-FA catalyst is significantly restricted, while glycerol pyrolysis was promoted on a high extent due to the presence of Ni active sites (Table 6). Moreover, the highest  $Y_{C2+}$  of 5.2% is obtained for Ni-FA compared to Ni- $FA^x$  catalysts (0.7–1.7%), indicating that the pyrolysis of ethylene and/or ethane over Ni-FA is also unfavorable. Higher  $Y_{CO_2}$  and  $CO_2/CO$  ratio are generally considered as a criterion to evaluate the activity of WGS reaction [59]. Compared to Ni-FA, the higher  $X_{GCG}$  and  $Y_{CO_2}$  were obtained for Ni- $FA^H$ , which indicates that the removal of sulfur favors the WGS reaction. Among the Ni- $FA^x$  catalysts, Ni- $FA^{H/Na}$  achieves the highest  $Y_{CO_2}$  of 63%, followed by Ni- $FA^{Na}$  (52.7%), Ni- $FA^H$  (52.1%), and Ni- $FA^{Na/H}$  (46.9%). The same tendency is also observed for the corresponding  $H_2/CO$  and  $CO_2/CO$  molar ratios. In addition to the active sites, the alkali environment (alkali treatment as final step) was found more beneficial for the catalytic reaction in comparison with the acid environment (acid treatment as final step), which was attributed to the formation of basic sites after alkali treatment [21]. Moreover, the formation of Ni-rich NiFe alloys was also responsible for the high molar ratio of  $H_2/CO$  and  $CO_2/CO$  for Ni- $FA^{H/Na}$ . However, the formation of Fe-rich NiFe alloy in Ni- $FA^{Na/H}$  results in the inhibition of the WGS reaction due to the loss of Ni active surface area. The  $CO_2$  selectivity over Ni- $FA^x$  catalysts matches well with both  $X_{GCG}$  and  $Y_{H2}$ , which in turn proves that the WGS has an important impact on the product distributions.

### 3.4. Characterization of used catalysts

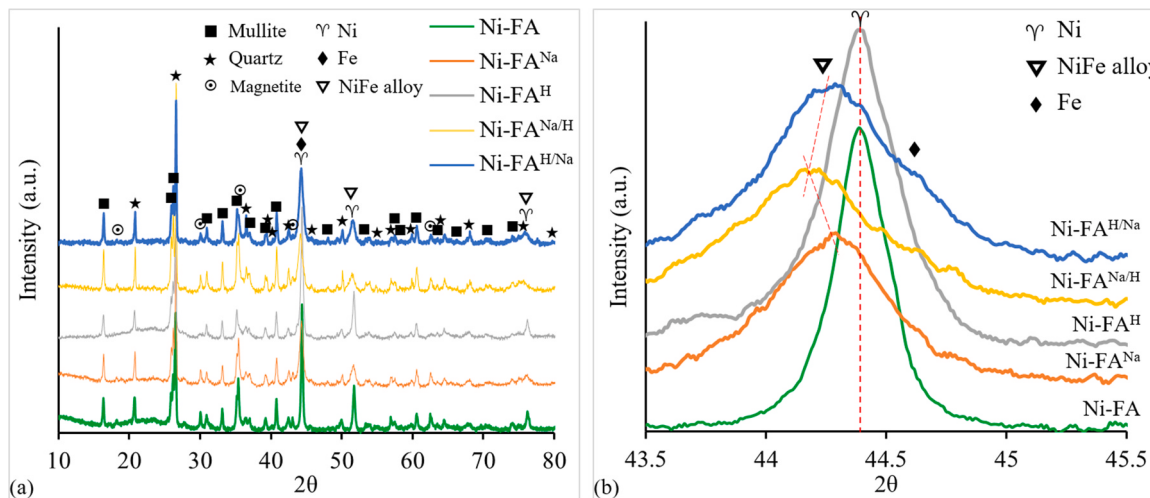
To better understand the GSR performance over Ni-FA and Ni- $FA^x$  catalysts, the used catalysts were further investigated in terms of structural changes, sintering phenomena, and coke deposition using different characterization techniques including  $N_2$  adsorption-desorption, XRD, TEM, TGA/DTG, TPO, and Raman analysis.

The BET surface area and the total pore volume of the used Ni-FA and Ni- $FA^x$  catalysts are presented in Table 7 ( $N_2$  adsorption-desorption isotherms given in Fig. S1d). Compared to the corresponding reduced catalysts (Table 4), a slight decrease in the BET surface area occurs for the used Ni-FA (from 2.42 to 2.05  $m^2 \cdot g^{-1}$ ), Ni- $FA^{Na}$  (from 12.11 to 10.67  $m^2 \cdot g^{-1}$ ), and Ni- $FA^{H/Na}$  (from 12.73 to 9.18  $m^2 \cdot g^{-1}$ ). This could be attributed to a slight particle sintering and/or deformation. However, opposite results are found for the used Ni- $FA^H$  (from 2.69 to 14.29  $m^2 \cdot g^{-1}$ ) and Ni- $FA^{Na/H}$  (from 16.67 to 25.89  $m^2 \cdot g^{-1}$ ) samples. The significant increase of SSA could be ascribed to the formation of filamentous type carbonaceous species presenting high surface area. Nevertheless, no diffraction peak associated with coke was detected by XRD (Fig. 9). This might be due to the i) low amount of coke formation (below the XRD detection limit), and/or ii) the overlap of coke diffraction peaks with that of mullite phase (26.1°).

For the XRD results of the used catalysts (Fig. 9), it can be seen that  $Ni^\circ$  active sites maintain their metallic state under the GSR operating conditions. However, new reflection peaks at  $2\theta = 18.29^\circ$ ,  $30.08^\circ$ ,  $35.43^\circ$ ,  $43.05^\circ$ , and  $62.52^\circ$  were assigned to the magnetite ( $Fe_3O_4$ ) (ICDD file 96-900-6195). The formation of magnetite could be attributed to the appropriate oxidization of the metallic Fe by the oxygen species derived from activated water (as reforming oxidant,  $H_2O + * (active site) \leftrightarrow H_2 + O^*$ ) [33,57,60]. The existence of magnetite has been reported to favor the WGS reaction in the GSR process (Fig. 8a). In addition, it is worth mentioning that the diffraction peak of the anhydrite phase at 25.45° was not found in the used Ni-FA catalyst. Based on its GSR performance, one might speculate that the anhydrite was reduced (to  $CaS$ ) and then adsorbed on the surface of Ni active sites to form Ca-S-Ni during GSR [45]. This is a plausible interpretation of the deactivation of Ni-FA by catalytic poisoning. The crystalline sizes of the metallic particles ( $Ni^\circ$  and NiFe alloys) on the used Ni-FA and Ni- $FA^x$  catalysts were calculated using the Scherrer equation. Table 7 shows an increase in the  $Ni^\circ$  and NiFe alloys sizes after the GSR test, which could be attributed to the minor crystal sintering and/or the oxidation of iron (NiFe transformation to  $Ni-Fe_xO_y$ ) [25]. This is consistent with the BET

**Table 7**The physicochemical properties of the used Ni-FA and Ni-FA<sup>X</sup> catalysts.

catalysts	surface area ( $\text{m}^2 \cdot \text{g}^{-1}$ )	total pore volume ( $\text{cm}^3 \cdot \text{g}^{-1}$ )	average pore size (nm)	crystal size (nm) <sup>a</sup>	$R_{\text{coke}}$ ( $\text{mg}_{\text{coke}} \cdot \text{g}_{\text{catalyst}}^{-1} \cdot \text{h}^{-1}$ ) <sup>b</sup>	$R_{\text{carbon}}$ ( $\text{mg}_{\text{carbon}} \cdot \text{g}_{\text{catalyst}}^{-1} \cdot \text{h}^{-1}$ ) <sup>c</sup>
Ni-FA	2.05	0.04	79.00	46.35	6.94	9.52
Ni-FA <sup>Na</sup>	10.67	0.11	40.47	30.38	10.81	12.41
Ni-FA <sup>H</sup>	14.29	0.13	35.41	41.34	30.08	38.24
Ni-FA <sup>Na/H</sup>	25.89	0.26	40.31	24.48	21.44	25.93
Ni-FA <sup>H/Na</sup>	9.18	0.13	57.95	26.64	5.16	6.32

<sup>a</sup> The crystal size of Ni<sup>o</sup> in used Ni-FA and Ni-FA<sup>H</sup> catalysts, and NiFe alloys in other catalysts.<sup>b</sup>  $R_{\text{coke}}$  (Eq. 9) was obtained by TGA analysis after 3 h GSR (coke is the mixture of elemental C, H, O, etc. [26]).<sup>c</sup>  $R_{\text{carbon}}$  (Eq. 10) data was obtained using *in-situ* TPO analysis after 3 h GSR (carbon refers to the elemental C).Fig. 9. XRD patterns of the used Ni-FA and Ni-FA<sup>X</sup> catalysts.

results. Moreover, the trend of metallic particle sizes similar to that of the corresponding reduced catalysts (Table 4), following the order of Ni-FA > Ni-FA<sup>H</sup> > Ni-FA<sup>Na</sup> > Ni-FA<sup>H/Na</sup> > Ni-FA<sup>Na/H</sup>. This tendency was attributed to the formation of NiFe alloys within alkali-LPD Ni-FA<sup>X</sup> samples, which decrease the surface mobility of Ni particles and weaken the particle agglomeration and sintering. Due to the existence of more Fe-rich NiFe alloy (lower 2θ in Fig. 9b), Ni-FA<sup>Na/H</sup> possesses the smallest particle size.

TEM was performed to examine the particle size distribution. Fig. 10 shows that the metallic particles are homogeneously distributed on the surface of the alkali-LPD FA<sup>X</sup> supports. As compared to the corresponding reduced samples (Fig. 7), the average metallic particle size shows a slight growth for the used Ni-FA (from 42.9 to 51.6 nm), Ni-FA<sup>H</sup> (from 36.6 to 38.7 nm), Ni-FA<sup>Na</sup> (from 26.7 to 27.7 nm), Ni-FA<sup>H/Na</sup> (from 26.1 to 26.8 nm), except for Ni-FA<sup>Na/H</sup> (25.5 nm, unchanged). As discussed above (XRD analysis in §3.4), this increase is a result of minor deformation and/or aggregation of metal particles. Notably, the average size of metallic particles measured via TEM analysis is slightly different from that measured by XRD, probably due to different calculation mechanism [61]. Nevertheless, a similar variation trend (Ni-FA > Ni-FA<sup>H</sup> > Ni-FA<sup>Na</sup> > Ni-FA<sup>H/Na</sup> > Ni-FA<sup>Na/H</sup>) was obtained. Moreover, the average rate of sintering (Eq. 8) gives the following order of Ni-FA ( $6.8\% \cdot \text{h}^{-1}$ ) > Ni-FA<sup>H</sup> ( $1.9\% \cdot \text{h}^{-1}$ ) > Ni-FA<sup>Na</sup> ( $1.2\% \cdot \text{h}^{-1}$ ) > Ni-FA<sup>H/Na</sup> ( $0.9\% \cdot \text{h}^{-1}$ ) > Ni-FA<sup>Na/H</sup> ( $0.05\% \cdot \text{h}^{-1}$ ). Compared to Ni-FA and Ni-FA<sup>H</sup>, the lower sintering rate of metallic particles for Ni-FA<sup>Na</sup>, Ni-FA<sup>H/Na</sup>, and Ni-FA<sup>Na/H</sup> indicates that alkali-LPD FA<sup>X</sup> materials offer the metallic particles a more effective resistance to sintering. This was attributed to the formation of the NiFe alloys (§3.2), which suppresses the migration of active metals. Particularly, the minimum change observed for Ni-FA<sup>Na/H</sup> could be attributed to the highest amount of iron and the highest specific surface area, which could provide more space and form

more NiFe alloy species.

Furthermore, the morphology of the coke formed on the used catalysts is illustrated in Fig. 10. In comparison to Ni-FA, Ni-FA<sup>Na</sup>, and Ni-FA<sup>H/Na</sup> catalysts, the presence of more filamentous type coke on the surface of Ni-FA<sup>H</sup> and Ni-FA<sup>Na/H</sup> catalysts was confirmed by TEM analysis (Fig. 10c-d). This could indicate that the acid treatment (as the final processing) for FA could induce the formation of filamentous type coke probably due to the formation of acidic sites [55,62]. The existence of filamentous coke is in line with the increase of BET surface area for Ni-FA<sup>H</sup> and Ni-FA<sup>Na/H</sup> (Table 7). Filamentous coke has been generally reported as a result of carbon diffusion in metallic sites and subsequent nucleation of adsorbed carbon atoms [26]. In Fig. 10c-d, the metallic particles located on the tip of filamentous coke are clearly observed. Nevertheless, the fact that filamentous coke has less impact on Ni<sup>o</sup> catalytic activity has been clarified by many researchers on account of the accessibility of the surface of the active sites to the reactants. Meanwhile, the growth of filamentous coke observed in TEM images could generate the rearrangement of the Ni active sites on the support surface [58], which could impact their catalytic behavior during GSR. This could interpret the higher catalytic activity of Ni-FA<sup>H</sup> (Fig. 8b) and lower average rate of sintering ( $1.9\% \cdot \text{h}^{-1}$ ) compared to Ni-FA. Additionally, the width of the filamentous coke on Ni-FA<sup>H</sup> is higher than that of Ni-FA<sup>Na/H</sup>, which is probably due to the larger Ni particle size in the former catalyst (38.7 nm) [63].

The amount and type of the coke formed on the used Ni-FA and Ni-FA<sup>X</sup> catalysts were determined by TGA and the results are shown in Fig. 11a. The obvious difference is attributed to the co-oxidation of different amounts of reducible species (nickel, iron, and carbonaceous). To eliminate the increase of mass generated by the oxidation of reduced species, TGA analysis was also performed for the reduced Ni-FA and Ni-FA<sup>X</sup> catalysts (Fig. S7). Consequently, the coke formation rate was

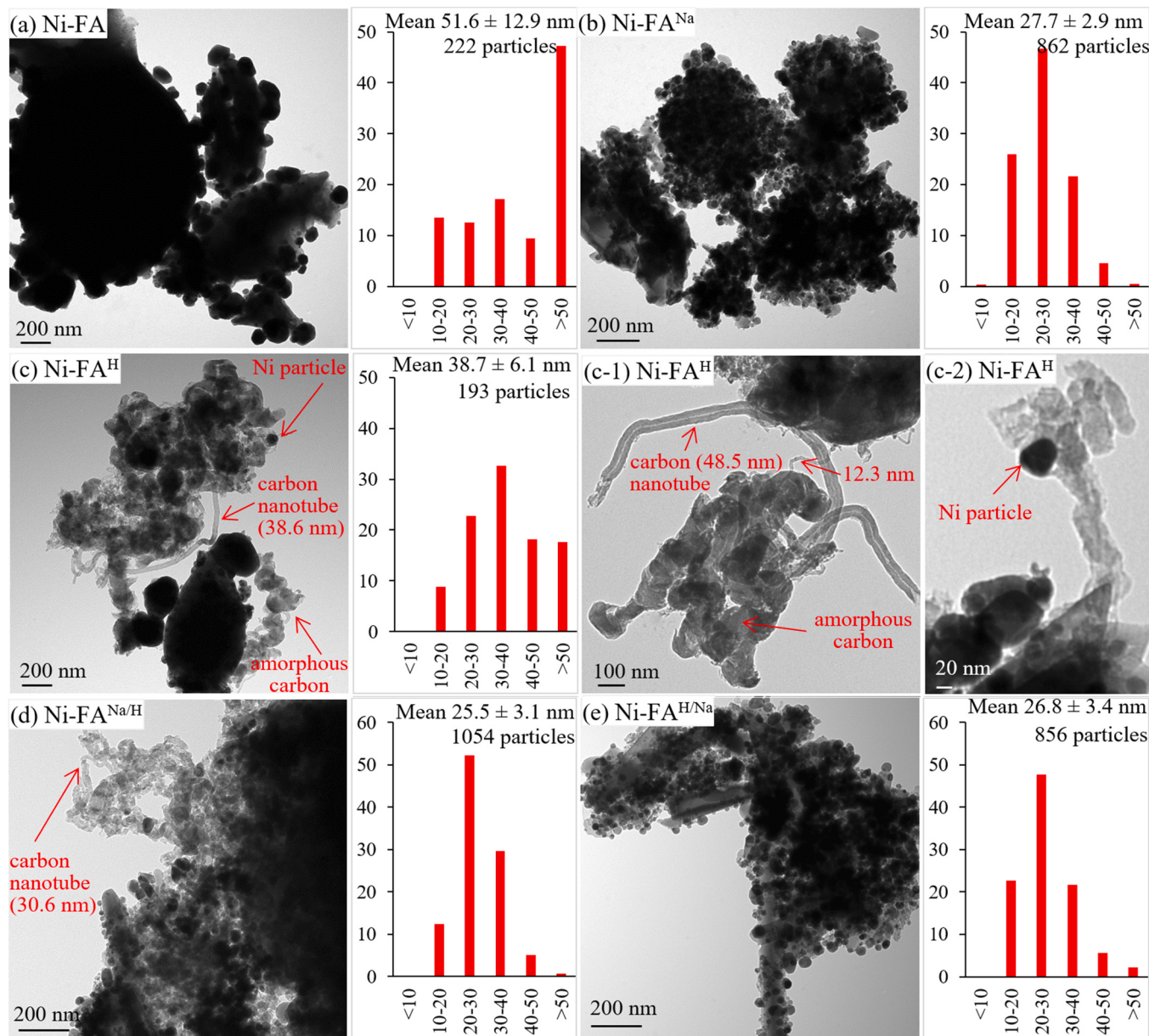


**Fig. 10.** The TEM images of the used Ni-FA and Ni-FA<sup>x</sup> catalysts, (a) Ni-FA, (b) Ni-FA<sup>Na</sup>, (c, c-1, and c-2) Ni-FA<sup>H</sup>, (d) Ni-FA<sup>Na/H</sup>, and (e) Ni-FA<sup>H/Na</sup>.

calculated (Eq. 9) to be 6.94, 10.81, 30.08, 21.44, and 5.16 mg<sub>coke</sub> • g<sub>catalyst</sub><sup>-1</sup> • h<sup>-1</sup> for the Ni-FA, Ni-FA<sup>Na</sup>, Ni-FA<sup>H</sup>, Ni-FA<sup>Na/H</sup>, and Ni-FA<sup>H/Na</sup>, respectively (Table 7). Coke is reported to cover heavy hydrocarbons and/or oxygenates [26], which would interfere with the value of elemental carbon balance (Eqs. 4–5) in glycerol conversion based on the TGA result. Besides, the amount of coke as mentioned above TGA analysis might be lower than the actual values, considering the coke residing on the reactor wall and the oxidation of the partially reduced species during GSR (Fig. 9). In this context, the *in-situ* TPO approach (as described in §2.2.5, Eq. 10) was considered in the present work to accurately estimate the amount of carbon formed on the used catalysts (Fig. 11b). By measuring the concentration of C-containing gases in the reactor effluent using a MicroGC, the average rate of elemental carbon was calculated to be 9.52, 12.41, 38.24, 25.93, and 6.32 mg<sub>carbon</sub> • g<sub>catalyst</sub><sup>-1</sup> • h<sup>-1</sup> for Ni-FA, Ni-FA<sup>Na</sup>, Ni-FA<sup>H</sup>, Ni-FA<sup>Na/H</sup>, and Ni-FA<sup>H/Na</sup> catalysts, respectively (Table 7). It was found that both TGA and *in-situ* TPO analysis shows the same order of Ni-FA<sup>H</sup> > Ni-FA<sup>Na/H</sup> > Ni-FA<sup>Na</sup> > Ni-FA > Ni-FA<sup>H/Na</sup>, which is consistent with the TEM

observation. The lower coke formation on Ni-FA, Ni-FA<sup>Na</sup>, and Ni-FA<sup>H/Na</sup> could be explained as following: for the first (Ni-FA) catalyst, the sulfur-poisoning leads to a lower catalytic activity during GSR, which reduces the risk of coke deposition [63], while for Ni-FA<sup>Na</sup> and Ni-FA<sup>H/Na</sup> the less amount of coke could be attributed to the presence of the alkali/alkaline oxides (alkali treatment as final step) resisting to coke formation/deposition [64,65].

In addition to quantitative analysis, DTG and TPO could provide qualitative information on the coke type. In the DTG profile (Fig. 11a), the peak at low temperature (ca. 500 °C) is related to the burning of amorphous (disordered) coke, the shoulder peak at 545 °C corresponds to the oxygenated coke, and the high temperature peak (585–590 °C) matches the more ordered coke. Due to the less amount of coke formed on Ni-FA and Ni-FA<sup>H/Na</sup>, a broad irregular curve is observed in their DTG profiles. A similar result is achieved in the analysis of the *in-situ* TPO-MicroGC profiles (Fig. 11b). For all used samples, the CO<sub>2</sub> evolution is initiated at about 300 °C, while the peaks appear at different temperatures. For Ni-FA<sup>H</sup>, Ni-FA<sup>Na/H</sup>, and Ni-FA<sup>Na</sup>, two main features are observed, including a relatively intense peak at ca. 595 °C (ordered

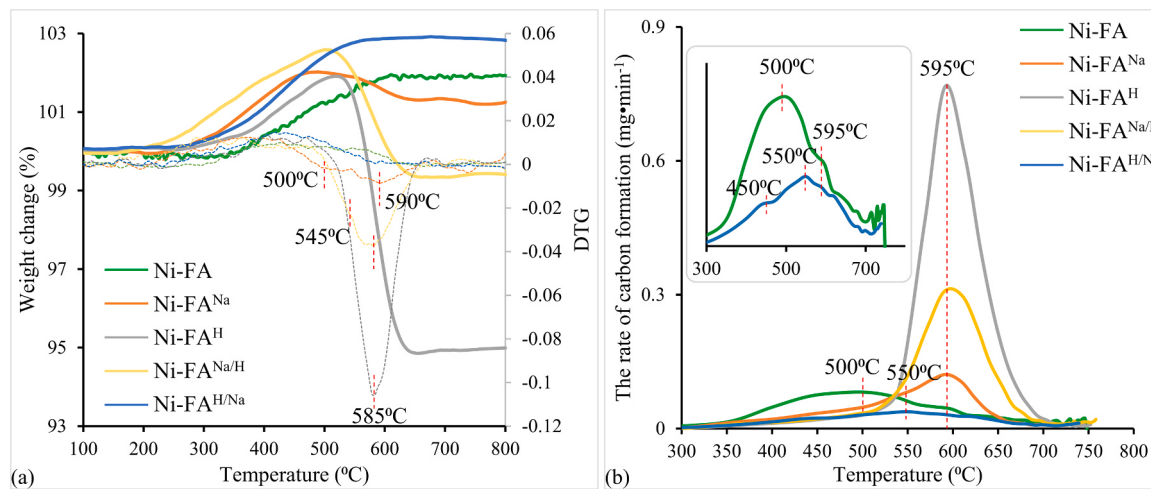


Fig. 11. TGA/DTG and in-situ TPO-MicroGC results of the used Ni-FA and Ni-FA<sup>x</sup> catalysts.

carbon) and a weaker broad tail from 300 °C to 525 °C (amorphous carbon). The *in-situ* TPO profiles of Ni-FA and Ni-FA<sup>H/Na</sup> display broad peaks in the range of 300–700 °C, as well as two shoulder peaks at 450 °C and 595 °C. However, the maximum peak of Ni-FA shifted from 500 °C to 550 °C when FA undergone two-step HNO<sub>3</sub>/NaOH treatment. As reported in the literature, the amorphous coke is generally oxidized in the region of 300–530 °C and the oxidation of carbonaceous deposits with different graphitization degrees occurs above 530 °C [15,26,66]. The present results indicate the existence of a series of coke with different crystallinity (transition from amorphous to ordered carbon) on the surface of used catalysts. Obviously, more structurally ordered coke is formed on the surface of Ni-FA<sup>H</sup>, Ni-FA<sup>Na/H</sup>, and Ni-FA<sup>Na</sup>. In contrast, more amorphous coke is generated on the surface of Ni-FA<sup>H/Na</sup> and Ni-FA. The internal structures of the coke species deposited on the used catalysts are further investigated by Raman analysis to better understand the different microcrystalline structures.

Fig. 12 illustrates the Raman spectra of the coke formed on the used Ni-FA and Ni-FA<sup>x</sup>, which were deconvoluted to three bands (D<sub>1</sub>, D<sub>2</sub>, and G) assignment [67]. Two strong peaks at about 1350 cm<sup>-1</sup> (D<sub>1</sub> band) and 1589 cm<sup>-1</sup> (G band) are shown for each sample. The G band at 1589 cm<sup>-1</sup> is assigned to the stretching vibration with E<sub>2g</sub> symmetry in the graphite layer (crystalline carbon structure) [63,67,68]. The D<sub>1</sub> band

at 1350 cm<sup>-1</sup> corresponds to the lattice vibration with A<sub>1g</sub> symmetry due to the in-plane defects and heteroatoms. This band (D<sub>1</sub>) can also be attributed to aromatic clusters having more than 6 rings (amorphous carbon structure). The D<sub>2</sub> band centered at ca. 1500 cm<sup>-1</sup> was observed for Ni-FA<sup>H</sup>, Ni-FA<sup>Na/H</sup>, and Ni-FA<sup>Na</sup>, and is suggested to originate from amorphous sp<sup>2</sup>-bonded forms of carbon (represented as functional groups and small aromatic clusters) [67,69]. Based on Raman peak intensities, the coke formed on the used catalysts follows quantitatively the order of Ni-FA<sup>H</sup> > Ni-FA<sup>Na/H</sup> > Ni-FA<sup>Na</sup> > Ni-FA<sup>H/Na</sup> > Ni-FA. This result is similar to TGA and TPO results. The relative intensity ratio of D<sub>1</sub> and G bands (I<sub>D1</sub>/I<sub>G</sub>) could reflect the degree of graphitization of the coke deposited on the catalysts, which means that a higher crystallinity results in lower I<sub>D1</sub>/I<sub>G</sub> values. As can be seen in Fig. 12, the I<sub>D1</sub>/I<sub>G</sub> ratio for Ni-FA<sup>H</sup> (0.63), Ni-FA<sup>Na/H</sup> (0.71), and Ni-FA<sup>Na</sup> (0.72) is significantly lower than for Ni-FA<sup>H/Na</sup> (1.77) and Ni-FA (1.37). This implies that a larger proportion of structurally ordered coke was formed on the used Ni-FA<sup>H</sup>, Ni-FA<sup>Na/H</sup>, and Ni-FA<sup>Na</sup> catalysts.

### 3.5. Catalytic stability of Ni-FA<sup>H/Na</sup> catalyst

In addition to activity/selectivity, the stability is another pivotal property of catalysts for long-term operation. According to the GSR performance (discussed in §3.3) and characterization results (§3.2 and §3.4) of Ni-FA<sup>x</sup> catalysts, the best catalyst (Ni-FA<sup>H/Na</sup>, with X<sub>GCG</sub> = 99.2%, Y<sub>H2</sub> = 74.5%), and the lowest carbon formation rate of 6.32 mg<sub>carbon</sub> • g<sub>catalyst</sub><sup>-1</sup> • h<sup>-1</sup> was chosen to investigate the stability during 1500 min TOS to further evaluate its potential for industrial applications (Fig. 13).

As seen from Fig. 13a, the high H<sub>2</sub> yield (73.2%) and glycerol conversion (X<sub>GCG</sub> = 98.5%) remain very stable during the 1500 min GSR. In addition, very low average rates of carbon formation (*in-situ* TPO analysis) can be observed after 180 min (6.32 mg<sub>carbon</sub> • g<sub>catalyst</sub><sup>-1</sup> • h<sup>-1</sup>) and 1500 min (8.52 mg<sub>carbon</sub> • g<sub>catalyst</sub><sup>-1</sup> • h<sup>-1</sup>). The characterization of coke after 180 min TOS was discussed in §3.4. The morphologies of the used Ni-FA<sup>H/Na</sup> are similar after 180 min (Fig. 10e) and 1500 min GSR reaction (Fig. 13b). Only a slight change of metallic particle size was detected with the increase of TOS to 1500 min, from 26.8 nm (Fig. 10e) to 29.1 nm (Fig. 13b). These results confirm a very good stability of Ni-FA<sup>H/Na</sup> in a long-term GSR operation. Furthermore, its GSR performance is comparable with various catalysts with different supports reported in the literature at similar temperatures (600–650 °C) (Table 8). The catalytic conversion rate of Ni-FA<sup>H/Na</sup> shows its clear advantage among the recorded materials.

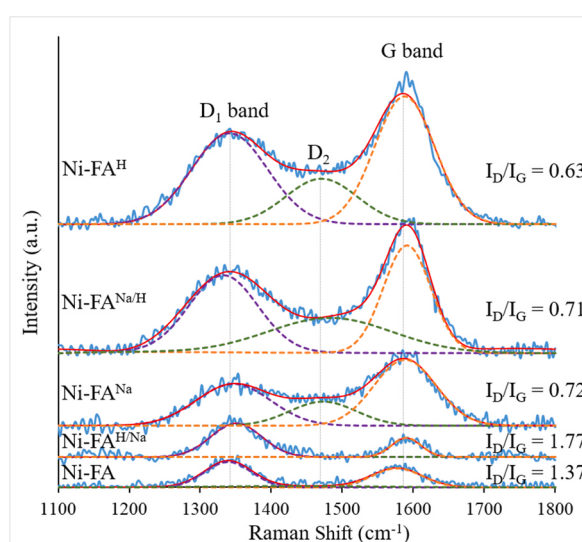
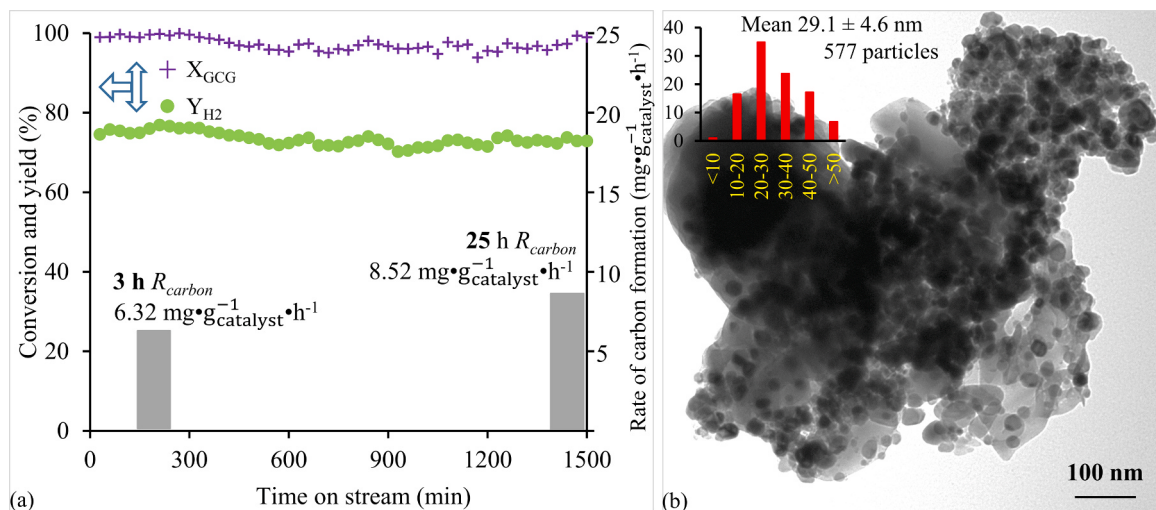


Fig. 12. Raman spectrum of coke formed on the used Ni-FA and Ni-FA<sup>x</sup> catalysts.



**Fig. 13.** Time-on-stream dependence of GSR reaction over Ni-FA<sup>H/Na</sup> catalyst: (a) glycerol conversion to gas products ( $X_{\text{GCG}}$ ),  $\text{H}_2$  yield ( $Y_{\text{H}_2}$ ), and the average rate of carbon formation ( $R_{\text{carbon}}$ ), and (b) TEM image of the used catalyst. [Reaction conditions:  $T = 630 \text{ }^{\circ}\text{C}$ ,  $P = 1 \text{ atm}$ , WHSV =  $7.37 \text{ h}^{-1}$ , S/C = 3; TOS = 1500 min].

**Table 8**  
Comparison of the GSR performance of Ni-based catalysts in different studies.

Ni loading (wt%)	support	synthesis method <sup>a</sup>	reforming condition				glycerol conversion (%)	$\text{H}_2$ yield (%)	Ref.
			S/C <sup>b</sup>	T ( $^{\circ}\text{C}$ )	WHSV ( $\text{h}^{-1}$ )	t (h)			
15	$\text{Al}_2\text{O}_3$	IWI	2	650	6.61	4	78	38.6	[70]
10	$\text{SiO}_2$	WI	1	600	19.12	5	52	31.4	[71]
8	$\text{SiO}_2$	WI	3	625	37.45	1	85	43.6	[72]
8	$\gamma\text{-Al}_2\text{O}_3$	WI	6.8	650	37.45	1	94	39	[73]
8	$\text{Al}_2\text{O}_3$	WI	3	625	37.45	1	~88	22.9	[72]
9.6	MgO	IWI	2	650	22.04	2	100	52	[74]
8	$\text{ZrO}_2$	WI	3	625	37.45	1	~90	37.1	[72]
12	$\text{CeO}_2$	IWI	4	600	42.51	2	99	74.7	[74]
15	$\text{CeO}_2$	IWI	5	650	6.32	4	83.3	68.9	[70]
12.7	$\text{TiO}_2$	IWI	2	650	22.04	2	84	47	[74]
10	$\text{La}_2\text{O}_3$	WI	1	600	19.12	5	26	8.6	[71]
5	LFSO <sup>c</sup>	WI	6.8	650	37.45	1	~93.5	60	[75]
8	ATP <sup>d</sup>	WI	3	600	37.45	20	~62.5	~14.3	[76]
7.5	FA <sup>H/Na</sup>	SSI	3	630	7.37	25	99	73.2	present work

<sup>a</sup> Incipient wetness impregnation (IWI), wet impregnation (WI), solid state impregnation (SSI).

<sup>b</sup> Molar ratio of steam to carbon in the feed.

<sup>c</sup>  $\text{La}_{9.83}\text{Si}_{4.5}\text{Fe}_{1.5}\text{O}_{26 \pm \delta}$  apatite.

<sup>d</sup> Attapulgite.

### 3.6. Correlation between catalyst features and GSR performance

Some noteworthy features can be highlighted based on the characteristics of the investigated Ni-FA and Ni-FA<sup>x</sup> catalysts (pre-reaction §3.1–3.2 and post-reaction §3.4) and the corresponding GSR performance (§3.3 and §3.5). The superior GSR performance of Ni-FA<sup>H/Na</sup> is associated with *i*) the low sulfur-containing species resisting catalyst poison, due to removal via acid washing, *ii*) the high specific surface area and pore volume providing more space for  $\text{Ni}^\circ$  dispersion, due to disintegration of aluminosilicate (glassy) structure in alkali treatment, *iii*) the intimate interaction of Ni with FA diminishing sintering of Ni particles, which offers a stable catalytic performance due to the exposure of Fe-containing species after alkali washing, thus resulting in the formation of NiFe alloys after reduction, and *iv*) the low amount of coke deposition when the alkali treatment is the end process. In terms of GSR performance, Ni-FA<sup>H/Na</sup> was followed by Ni-FA<sup>Na</sup> due to the absence of acid treatment, resulting in sulfur-containing residues that negatively impact the activity of Ni-FA<sup>Na</sup>. Even though an acid treatment was applied in the case of Ni-FA<sup>Na/H</sup> and Ni-FA<sup>H</sup>, more coke was found to be generated because the acidic environment (acid treatment is the end step) favors the cracking and polymerization of hydrocarbons to

carbonaceous precursors, which was the main reason influencing their catalytic behavior in GSR. However, the rearrangement of  $\text{Ni}^\circ$  particles over the Ni-FA<sup>H</sup> catalyst could increase the  $\text{Ni}^\circ$  active surface area during the GSR due to the growth of filamentous coke and the weak metal-support interaction, which was responsible for its slightly higher catalytic performance compared to Ni-FA<sup>Na/H</sup>. In addition, the reduction of Ni active surface area caused by the formation of more Fe-rich NiFe alloy in Ni-FA<sup>Na/H</sup> weakened the WGS reaction.

### 4. Conclusions

We have confirmed the FA residue as a potential promising support. Based on our previous work, not all kinds of as-received FA are suitable as support. Low-Ca/S FA residues with a high surface area deserve greater attention. Therefore, we investigated the effect of acid/alkali treatment procedures on the properties of FA to improve the catalytic activity of FA-supported Ni-based catalysts that convert glycerol to hydrogen through steam reforming. The significant results of this work can be summarized as:

- 1) Four treatment procedures were carried out to modify the physicochemical properties of FA. In these procedures,  $\text{FA}^x$  was obtained through one-step acid or alkali treatment, as well as two-step acid/alkali treatment. Furthermore, the sequence of the acid and alkali treatment processing was first considered in the present work.
- 2) The catalytic activity of the  $\text{Ni-FA}^x$  catalysts was significantly improved when the FA underwent activation in terms of acid and/or alkali solution. According to the results, the impurities (mainly sulfur-containing species) within as-received FA have a poisoning effect on the active metal (Ni) resulting in a weak catalytic activity, which could be effectively removed by acid solution. On the other hand, both BET surface area and pore volume were considerably improved when alkali solution was applied in the activation process. The dissolution of silica in NaOH solution, which resulted in the breakage of the Si-Al skeleton of FA, offered more space for Ni dispersion. Simultaneously, more iron-containing species within FA emerged after alkali treatment, resulting in the formation of  $\text{Ni}_x(\text{Fe})_y\text{O}$  mixed oxides after Ni incorporation, which caused a more intimate interaction between Ni and Fe containing species. This noticeably affected the reducibility of nickel oxides and led to the formation of NiFe alloys after reduction. However, the NiFe alloy was not produced in acid-treated  $\text{FA}^H$ . Compared to one-step acid or alkali treatment, two-step processing was noted to obtain higher BET surface area and pore volume because more ingredients (Si, Al, Ca, Fe, K, S, etc.) within FA were dissolved.
- 3) We highlighted for the first time the effect of the sequence of the acid and alkali solution during two-step processing on the physicochemical properties of the FA and its supported Ni catalytic performance in GSR. Alkali treatment as initial step could provide more reaction surface for the subsequent acid washing, resulting in higher surface area and pore volume for  $\text{FA}^{\text{Na}/\text{H}}$  compared to those of  $\text{FA}^{\text{H}/\text{Na}}$  sample. Moreover, the new crystallite (hydroxy sodalite) formed during alkali washing could be further dissolved by following acid treatment, leading to an obvious decrease in the silica and alumina content. However, acid washing as the first-step operation did not behave as alkali due to the insolubility of the core ingredients of FA in acid solution. Therefore, the chemical composition was successfully adjusted. After Ni incorporation, similar qualitative results (TPR and TEM) were found for  $\text{Ni-FA}^{\text{Na}/\text{H}}$  and  $\text{Ni-FA}^{\text{H}/\text{Na}}$  catalysts. However, more  $\text{Ni}^\circ$  active sites (higher Ni dispersion for a same Ni loading) were achieved by  $\text{Ni-FA}^{\text{H}/\text{Na}}$  in comparison to the  $\text{Ni-FA}^{\text{Na}/\text{H}}$  samples, which directly affected their catalytic performance for GSR reaction.
- 4) Among the five as-prepared catalysts, the  $\text{Ni-FA}^{\text{H}/\text{Na}}$  sample displayed the best  $\text{Ni}^\circ$  dispersion (proved by  $\text{H}_2$ -pulse chemisorption and TEM) and showed superior glycerol conversion to gaseous product (99.2%), hydrogen yield (74.5%),  $\text{H}_2/\text{CO}$  (5.7) and  $\text{CO}_2/\text{CO}$  (2.1) molar ratios compared to the Ni supported on the untreated FA (54.1%, 22.8%, 1.4, 0.14, respectively). According to the BET, XRF, XRD, TPR, XPS, and TEM analysis results, several other features (e.g., chemical composition, surface area, reducibility, and particle size) also contributed to the outstanding improvement of the catalytic performance of  $\text{Ni-FA}^{\text{H}/\text{Na}}$ .
- 5) The characterization of the used catalysts by a combination of BET, TEM, TGA/DTG, *in-situ* TPO, and Raman analyses revealed that the lowest amount of coke (amorphous) was formed over  $\text{Ni-FA}^{\text{H}/\text{Na}}$  ( $6.32 \text{ mg}_{\text{carbon}} \cdot \text{g}_{\text{catalyst}}^{-1} \cdot \text{h}^{-1}$ ). Both WGS and reverse Boudouard reactions are favorable when the catalyst was treated by alkali solution as final step. However, more coke was found for  $\text{Ni-FA}^H$  and  $\text{Ni-FA}^{\text{Na}/\text{H}}$  because the acidic environment favors cracking and polymerization of hydrocarbons to coke precursors. The results of XRD and TEM confirmed that the formation of NiFe alloys in Ni-based supported alkali-LPD FA<sup>x</sup> ( $\text{Ni-FA}^{\text{Na}}$ ,  $\text{Ni-FA}^{\text{Na}/\text{H}}$ , and  $\text{Ni-FA}^{\text{H}/\text{Na}}$ ) was beneficial for the  $\text{Ni}^\circ$  metal anti-sintering.
- 6)  $\text{Ni-FA}^{\text{H}/\text{Na}}$  showed an excellent stability during 1500 min TOS with high H<sub>2</sub> yield (73.2%) and glycerol conversion ( $X_{\text{GCG}} = 98.5\%$ ), as well as a low average rate of carbon formation ( $8.52 \text{ mg}_{\text{carbon}} \cdot \text{g}_{\text{catalyst}}^{-1} \cdot \text{h}^{-1}$ ). In summary, the superior GSR performance of  $\text{Ni-FA}^{\text{H}/\text{Na}}$  is mainly attributed to the following features: *i*) removal of sulfur-containing species by the acid washing to avoid catalyst poison, *ii*) disintegration of aluminosilicate (glassy) structure within FA by extraction of Si-containing species after alkali treatment, which increases the specific surface area and consequently provides more space for  $\text{Ni}^\circ$  dispersion, *iii*) intimate interaction of Ni with FA, due to the exposure of Fe-containing species after alkali washing resulting in the formation of Ni/Fe mixed oxides, which leads to the transformation into NiFe alloys after reduction and enhances metal-support interaction, thus diminishing sintering of Ni particles and offering a stable catalytic performance, and *iv*) high resistance to coke formation when alkali treatment is the end process.

In short, the present work demonstrates that the catalytic efficiency of low activity FA can be significantly improved through acid washing prior to alkali treatment, making this residual material an appealing support to develop Ni-based catalysts. The two-step acid/alkali treatment not only led to the removal of sulfur-containing species but also increases the surface area of FA, whilst maintaining its thermostability for long-term operation. The present work could open the window to further innovative ideas regarding the application of modified FAs in other catalytic processes, such as partial oxidation (bio-methanol), transesterification (biodiesel), Fischer-Tropsch (liquid hydrocarbon), etc.

#### CRediT authorship contribution statement

Kang Gao: Conceptualization, Methodology, Investigation, Validation, Writing- Original draft preparation, Visualization., Ommolbanin A. Sahraei: Validation, Writing- Original draft preparation., Maria C. Iliuta: Conceptualization, Validation, Supervision, Project administration, Resources, Writing- Reviewing and Editing, Funding acquisition.

#### Declaration of Competing Interest

The authors declare that they have no known competing financial interests or personal relationships that could have appeared to influence the work reported in this paper.

#### Acknowledgements

The authors acknowledge with thanks Thi Thanh Nguyet Vu, Desagnés Alex, and Thi Ngoc Mai Dang for their assistance in the experimental work. They also gratefully acknowledge the financial support from the Natural Sciences and Engineering Research Council of Canada (NSERC) and the China Scholarship Council (CSC, No. 201708130079).

#### Appendix A. Supporting information

Supplementary data associated with this article can be found in the online version at doi:10.1016/j.apcatb.2021.120791.

#### References

- [1] B.V. Ayodele, T.A.R.B.T. Abdullah, M.A. Alsaffar, S.I. Mustapa, S.F. Salleh, Recent advances in renewable hydrogen production by thermo-catalytic conversion of biomass-derived glycerol: overview of prospects and challenges, Int. J. Hydrogen Energy 45 (2020) 18160–18185.
- [2] M.R. Monteiro, C.L. Kugelmeier, R.S. Pinheiro, M.O. Batalha, A. da Silva César, Glycerol from biodiesel production: technological paths for sustainability, Renew. Sustain. Energy Rev. 88 (2018) 109–122.

- [3] N.D. Charisiou, K. Polychronopoulou, A. Asif, M.A. Goula, The potential of glycerol and phenol towards H<sub>2</sub> production using steam reforming reaction: a review, *Surf. Coat. Technol.* 352 (2018) 92–111.
- [4] O.A.Z. Sahraei, K. Gao, M.C. Iliuta, Application of industrial solid wastes in catalyst and chemical sorbent development for hydrogen/syngas production by conventional and intensified steam reforming. *New Dimensions in Production and Utilization of Hydrogen*, Elsevier,, 2020, pp. 21–55.
- [5] J.S. Hargreaves, Catalysts derived from waste materials, *Catal.* 30 (2018) 1–20.
- [6] A. Laca, A. Laca, M. Díaz, Eggshell waste as catalyst: a review, *J. Environ. Manag.* 197 (2017) 351–359.
- [7] J.A. Bennett, K. Wilson, A.F. Lee, Catalytic applications of waste derived materials, *J. Mater. Chem. A* 4 (2016) 3617–3637.
- [8] P. Munnik, P.E. de Jongh, K.P. de Jong, Recent developments in the synthesis of supported catalysts, *Chem. Rev.* 115 (2015) 6687–6718.
- [9] A.R.K. Gollakota, V. Volli, C.-M. Shu, Progressive utilisation prospects of coal fly ash: a review, *Sci. Total Environ.* 672 (2019) 951–989.
- [10] A. Bhatt, S. Priyadarshini, A.A. Mohanakrishnan, A. Abri, M. Sattler, S. Techaphaphawit, Physical, chemical, and geotechnical properties of coal fly ash: a global review, *Case Stud. Constr. Mater.* 11 (2019), e00263.
- [11] Z.T. Yao, X.S. Ji, P.K. Sarker, J.H. Tang, L.Q. Ge, M.S. Xia, Y.Q. Xi, A comprehensive review on the applications of coal fly ash, *Earth-Sci. Rev.* 141 (2015) 105–121.
- [12] K. Gao, M. Shokrollahi Yancheshmeh, Je Duchesne, M.C. Iliuta, Valorization of coal fly ash as a stabilizer for the development of Ni/CaO-based bifunctional material, *ACS Sustain. Chem. Eng.* 8 (2020) 3885–3895.
- [13] A. Dindi, D.V. Quang, L.F. Vega, E. Nashef, M.R.M. Abu-Zahra, Applications of fly ash for CO<sub>2</sub> capture, utilization, and storage, *J. CO<sub>2</sub> Util.* 29 (2019) 82–102.
- [14] S. Scaccia, G. Vanga, D.M. Gattia, S. Stendardo, Preparation of CaO-based sorbent from coal fly ash cenospheres for calcium looping process, *J. Alloy. Compd.* 801 (2019) 123–129.
- [15] K. Gao, O.A. Sahraei, M.C. Iliuta, Development of residue coal fly ash supported nickel catalyst for H<sub>2</sub> production via glycerol steam reforming, *Appl. Catal. B* 291 (2021), 119958.
- [16] F. Zhang, S.R. Wang, J.H. Chen, Y.R. Wang, B. Ru, L.J. Zhu, Effect of coal ash on the steam reforming of simulated bio-oil for hydrogen production over Ni-y-Al<sub>2</sub>O<sub>3</sub>, *Bioresources* 11 (2016) 6808–6821.
- [17] S.R. Wang, F. Zhang, Q.J. Cai, L.J. Zhu, Z.Y. Luo, Steam reforming of acetic acid over coal ash supported Fe and Ni catalysts, *Int. J. Hydrogen Energy* 40 (2015) 11406–11413.
- [18] S.R. Wang, F. Zhang, Q.J. Cai, X.B. Li, L.J. Zhu, Q. Wang, Z.Y. Luo, Catalytic steam reforming of bio-oil model compounds for hydrogen production over coal ash supported Ni catalyst, *Int. J. Hydrogen Energy* 39 (2014) 2018–2025.
- [19] S.B. Wang, G.Q. Lu, H.Y. Zhu, Fly ash as support for Ni catalysts in carbon dioxide reforming of methane, *Chem. Lett.* 28 (1999) 385–386.
- [20] M. Lu, Z.H. Xiong, J.Q. Li, X. Li, K.J. Fang, T. Li, Catalytic steam reforming of toluene as model tar compound using Ni/coal fly ash catalyst, *Asia-Pac. J. Chem. Eng.* 15 (2020), e2529.
- [21] Y.C. Gao, J.G. Jiang, Y. Meng, A. Aihemaiti, T.Y. Ju, X.J. Chen, F. Yan, A novel nickel catalyst supported on activated coal fly ash for syngas production via biogas dry reforming, *Renew. Energy* 149 (2020) 786–793.
- [22] H.C. Zhou, Y. Cao, H.Y. Zhao, H.Y. Liu, W.P. Pan, Investigation of H<sub>2</sub>O and CO<sub>2</sub> reforming and partial oxidation of methane catalytic effects of coal char and coal ash, *Energy Fuels* 22 (2008) 2341–2345.
- [23] D. Sotiropoulos, A. Georgakopoulos, N. Kolovos, Impact of free calcium oxide content of fly ash on dust and sulfur dioxide emissions in a lignite-fired power plant, *J. Air Waste Manag Assoc.* 55 (2005) 1042–1049.
- [24] A. Fernández-Jiménez, I. García-Lodeiro, O. Maltseva, A. Palomo, Mechanical-chemical activation of coal fly ashes: an effective way for recycling and make cementitious materials, *Front. Mater.* 6 (2019) 51.
- [25] O.A. Sahraei, A. Desgagnés, F. Larachi, M.C. Iliuta, Ni-Fe catalyst derived from mixed oxides Fe/Mg-bearing metallurgical waste for hydrogen production by steam reforming of biodiesel by-product: investigation of catalyst synthesis parameters and temperature dependency of the reaction network, *Appl. Catal. B* 279 (2020), 119330.
- [26] A. Ochoa, J. Bilbao, A.G. Gayubo, P. Castaño, Coke formation and deactivation during catalytic reforming of biomass and waste pyrolysis products: a review, *Renew. Sustain. Energy Rev.* 119 (2020), 109600.
- [27] G.H. Bai, W. Teng, X.G. Wang, H. Zhang, P. Xu, Processing and kinetics studies on the alumina enrichment of coal fly ash by fractionating silicon dioxide as nano particles, *Fuel Process. Technol.* 91 (2010) 175–184.
- [28] Y. Zhang, Y. Tao, J. Huang, P. Williams, Influence of silica-alumina support ratio on H<sub>2</sub> production and catalyst carbon deposition from the Ni-catalytic pyrolysis/reforming of waste tyres, *Waste Manag. Res.* 35 (2017) 1045–1054.
- [29] S.S. Chang, B. Clair, J. Ruelle, J. Beauchêne, F. Di Renzo, F. Quignard, G.J. Zhao, H. Yamamoto, J. Gril, Mesoporosity as a new parameter for understanding tension stress generation in trees, *J. Exp. Bot.* 60 (2009) 3023–3030.
- [30] B. Deka, K.G. Bhattacharyya, Using coal fly ash as a support for Mn(II), Co(II) and Ni(II) and utilizing the materials as novel oxidation catalysts for 4-chlorophenol mineralization, *J. Environ. Manag.* 150 (2015) 479–488.
- [31] F. Yan, J.G. Jiang, M. Zhao, S.C. Tian, K.M. Li, T.R. Li, A green and scalable synthesis of highly stable Ca-based sorbents for CO<sub>2</sub> capture, *J. Mater. Chem. A* 3 (2015) 7966–7973.
- [32] M. Aissaoui, O.A.Z. Sahraei, M.S. Yancheshmeh, M.C. Iliuta, Development of a Fe/Mg-bearing metallurgical waste stabilized-CaO/NiO hybrid sorbent-catalyst for high purity H<sub>2</sub> production through sorption-enhanced glycerol steam reforming, *Int. J. Hydrogen Energy* 45 (2020) 18452–18465.
- [33] O.A.Z. Sahraei, F. Larachi, N. Abatzoglou, M.C. Iliuta, Hydrogen production by glycerol steam reforming catalyzed by Ni-promoted Fe/Mg-bearing metallurgical wastes, *Appl. Catal. B* 219 (2017) 183–193.
- [34] Z.M. Zhang, X. Hu, L.J. Zhang, Y. Yang, Q.Y. Li, H.L. Fan, Q. Liu, T. Wei, C.Z. Li, Steam reforming of guaiacol over Ni/Al<sub>2</sub>O<sub>3</sub> and Ni/SBA-15: Impacts of support on catalytic behaviors of nickel and properties of coke, *Fuel Process. Technol.* 191 (2019) 138–151.
- [35] G. Xu, X.M. Shi, Characteristics and applications of fly ash as a sustainable construction material: a state-of-the-art review, *Resour. Conserv. Recycl.* 136 (2018) 95–109.
- [36] R. Terborg, B. Hansen, S. Bohm, Combined EDX and micro XRF analysis on SEMs, *Microsc. Microanal.* 22 (2016) 438–439.
- [37] T. Henni, Synthesis of hydroxy-sodalite (“zeolite”) from waste coal ash, *Soil Sci. Plant Nutr.* 33 (1987) 517–521.
- [38] M.C. Mishra, N.G. Reddy, B.H. Rao, Potential of citric acid for treatment of extremely alkaline bauxite residue: effect on geotechnical and geoenvironmental properties, *J. Hazard. Toxic. Radioact. Waste* 24 (2020), 04020047.
- [39] S. Abelló, E. Bolshak, D. Montané, Ni-Fe catalysts derived from hydrotalcite-like precursors for hydrogen production by ethanol steam reforming, *Appl. Catal. A: Gen.* 450 (2013) 261–274.
- [40] O. Clause, B. Rebourg, E. Merlen, F. Trifiro, A. Vaccari, Preparation and characterization of nickel-aluminum mixed oxides obtained by thermal decomposition of hydrotalcite-type precursors, *J. Catal.* 133 (1992) 231–246.
- [41] B. Liu, H.J. Sun, T.J. Peng, Q. He, One-step synthesis of hydroxysodalite using natural bentonite at moderate temperatures, *Miner. -Basel* 8 (2018) 521.
- [42] H.S. Chen, Z. Zheng, Z.W. Chen, X.T. Bi, Reduction of hematite (Fe<sub>2</sub>O<sub>3</sub>) to metallic iron (Fe) by CO in a micro fluidized bed reaction analyzer: a multistep kinetics study, *Powder Technol.* 316 (2017) 410–420.
- [43] V. Palma, C. Ruocco, E. Meloni, A. Ricca, Renewable hydrogen from ethanol reforming over CeO<sub>2</sub>-SiO<sub>2</sub> based catalysts, *Catalysts* 7 (2017) 226–241.
- [44] J.C. Lu, Y.Q. Lei, G.P. Wan, Z.Q. Mei, J. Yu, Y. Zhao, S.F. He, Y.M. Luo, Weakening the metal-support strong interaction to enhance catalytic performances of alumina supported Ni-based catalysts for producing hydrogen, *Appl. Catal. B* 263 (2020), 118177.
- [45] M. Lu, Z.H. Xiong, K.J. Fang, X. Li, J.Q. Li, T. Li, Steam reforming of toluene over nickel catalysts supported on coal gangue ash, *Renew. Energy* 160 (2020) 385–395.
- [46] N.D. Charisiou, K.N. Papageridis, L. Tzounis, V. Sebastian, S.J. Hinder, M.A. Baker, M. AlKetbi, K. Polychronopoulou, M.A. Goula, Ni supported on CaO-MgO-Al<sub>2</sub>O<sub>3</sub> as a highly selective and stable catalyst for H<sub>2</sub> production via the glycerol steam reforming reaction, *Int. J. Hydrogen Energy* 44 (2018) 256–273.
- [47] U.Y. Qazi, C.Z. Yuan, N. Ullah, Y.F. Jiang, M. Imran, A. Zeb, S.J. Zhao, R. Javaid, A. W. Xu, One-step growth of iron-nickel bimetallic nanoparticles on FeNi alloy foils: highly efficient advanced electrodes for the oxygen evolution reaction, *ACS Appl. Mater. Interfaces* 9 (2017) 28627–28634.
- [48] A. Morales-Marín, J.L. Ayastuy, U. Iriarte-Velasco, M.A. Gutiérrez-Ortiz, Nickel aluminate spinel-derived catalysts for the aqueous phase reforming of glycerol: Effect of reduction temperature, *Appl. Catal. B* 244 (2019) 931–945.
- [49] L. Wang, D. Li, M. Koike, S. Koso, Y. Nakagawa, Y. Xu, K. Tomishige, Catalytic performance and characterization of Ni-Fe catalysts for the steam reforming of tar from biomass pyrolysis to synthesis gas, *Appl. Catal. A: Gen.* 392 (2011) 248–255.
- [50] Q. Han, M.U. Rehman, J. Wang, A. Rykov, O.Y. Gutiérrez, Y. Zhao, S. Wang, X. Ma, J.A. Lercher, The synergistic effect between Ni sites and Ni-Fe alloy sites on hydrodeoxygenation of lignin-derived phenols, *Appl. Catal. B* 253 (2019) 348–358.
- [51] P. Djinović, I.G. Osojnik Črnivec, B. Erjavec, A. Pintar, Influence of active metal loading and oxygen mobility on coke-free dry reforming of Ni-Co bimetallic catalysts, *Appl. Catal. B* 125 (2012) 259–270.
- [52] G. Sadanandan, N. Sreelaitha, M.V. Phanikrishna Sharma, S. Kishta Reddy, B. Srinivas, K. Venkateswarlu, T. Krishnudu, M. Subrahmanyam, V. Durga, Kumari, Steam reforming of glycerol for hydrogen production over Ni/SiO<sub>2</sub> catalyst, *ISRN. Chem. Eng.* 2012 (2012) 1–10.
- [53] H. Tanaka, R. Kaino, K. Okumura, T. Kizuka, Y. Nakagawa, K. Tomishige, Comparative study of Rh/MgO modified with Fe, Co or Ni for the catalytic partial oxidation of methane at short contact time. Part I: Characterization of catalysts, *Appl. Catal. A: Gen.* 378 (2010) 175–186.
- [54] D.G. Mustard, C.H. Bartholomew, Determination of metal crystallite size and morphology in supported nickel catalysts, *J. Catal.* 67 (1981) 186–206.
- [55] V.K. Jones, L.R. Neubauer, C.H. Bartholomew, Effects of crystallite size and support on the carbon monoxide hydrogenation activity/selectivity properties of iron/carbon, *J. Phys. Chem.* 90 (1986) 4832–4839.
- [56] M.S. Yancheshmeh, O.A. Sahraei, M. Aissaoui, M.C. Iliuta, A novel synthesis of NiAl<sub>2</sub>O<sub>4</sub> spinel from a Ni-Al mixed-metal alkoxide as a highly efficient catalyst for hydrogen production by glycerol steam reforming, *Appl. Catal. B* 265 (2020), 11835.
- [57] M.H. Zhu, I.E. Wachs, Iron-based catalysts for the high-temperature water-gas shift (HT-WGS) reaction: a review, *ACS Catal.* 6 (2016) 722–732.
- [58] L.F. Bobadilla, F. Romero-Sarria, M.A. Centeno, J.A. Odriozola, Promoting effect of Sn on supported Ni catalyst during steam reforming of glycerol, *Int. J. Hydrogen Energy* 41 (2016) 9234–9244.
- [59] G.W. Wu, S.R. Li, C.X. Zhang, T. Wang, J.L. Gong, Glycerol steam reforming over perovskite-derived nickel-based catalysts, *Appl. Catal. B* 144 (2014) 277–285.
- [60] S. Hu, L.M. He, Y. Wang, S. Su, L. Jiang, Q.D. Chen, Q.C. Liu, H.Y. Chi, J. Xiang, L. S. Sun, Effects of oxygen species from Fe addition on promoting steam reforming of toluene over Fe-Ni/Al<sub>2</sub>O<sub>3</sub> catalysts, *Int. J. Hydrogen Energy* 41 (2016) 17967–17975.

- [61] B. Wang, Y.Y. Xiong, Y.Y. Han, J.P. Hong, Y.H. Zhang, J.L. Li, F.L. Jing, W. Chu, Preparation of stable and highly active Ni/CeO<sub>2</sub> catalysts by glow discharge plasma technique for glycerol steam reforming, *Appl. Catal. B*. 249 (2019) 257–265.
- [62] A. Sharma, K. Srivastava, V. Devra, A. Rani, Modification in properties of fly ash through mechanical and chemical activation, *Chem. Sci. Int. J.* 2 (2012) 177–187.
- [63] Z.J. Yu, X. Hu, P. Jia, Z.M. Zhang, D.H. Dong, G.Z. Hu, S. Hu, Y. Wang, J. Xiang, Steam reforming of acetic acid over nickel-based catalysts: the intrinsic effects of nickel precursors on behaviors of nickel catalysts, *Appl. Catal. B*. 237 (2018) 538–553.
- [64] G.T. Wurzler, R.C. Rabelo-Neto, L.V. Mattos, M.A. Fraga, F.B. Noronha, Steam reforming of ethanol for hydrogen production over MgO-supported Ni-based catalysts, *Appl. Catal. A: Gen.* 518 (2016) 115–128.
- [65] N. Czuma, K. Zarebska, M. Motak, M.E. Gálvez, P. Da Costa, Ni/zeolite X derived from fly ash as catalysts for CO<sub>2</sub> methanation, *Fuel* 267 (2020), 117139.
- [66] A. Ochoa, A. Arregi, M. Amutio, A.G. Gayubo, M. Olazar, J. Bilbao, P. Castaño, Coking and sintering progress of a Ni supported catalyst in the steam reforming of biomass pyrolysis volatiles, *Appl. Catal. B*. 233 (2018) 289–300.
- [67] B.B. Bao, J.L. Liu, H. Xu, Z.Y. Wang, K. Zhang, Fabrication of spinel coating on Hp40 alloy and its inhibition effect on catalytic coking during thermal cracking of light naphtha, *Braz. J. Chem. Eng.* 35 (2018) 721–730.
- [68] X.L. Zhu, C.D. Sheng, Evolution of the char structure of lignite under heat treatment and its influences on combustion reactivity, *Energy Fuels* 24 (2010) 152–159.
- [69] K. Maliutina, A. Tahmasebi, J. Yu, Effects of pressure on morphology and structure of bio-char from pressurized entrained-flow pyrolysis of microalgae, *Data Brief.* 18 (2018) 422–431.
- [70] O. Parlar Karakoc, M.E. Kibar, A.N. Akin, M. Yildiz, Nickel-based catalysts for hydrogen production by steam reforming of glycerol, *Int. J. Environ. Sci. Technol.* 16 (2018) 5117–5124.
- [71] V.V. Thyssen, T.A. Maia, E.M. Assaf, Ni supported on La<sub>2</sub>O<sub>3</sub>–SiO<sub>2</sub> used to catalyze glycerol steam reforming, *Fuel* 105 (2013) 358–363.
- [72] N.D. Charisiou, K.N. Papageridis, G. Siakavelas, L. Tzounis, K. Kousi, M.A. Baker, S. J. Hinder, V. Sebastian, K. Polychronopoulou, M.A. Goula, Glycerol steam reforming for hydrogen production over nickel supported on alumina, zirconia and silica catalysts, *Top. Catal.* 60 (2017) 1226–1250.
- [73] N.D. Charisiou, G. Siakavelas, K.N. Papageridis, A. Baklavridis, L. Tzounis, K. Polychronopoulou, M.A. Goula, Hydrogen production via the glycerol steam reforming reaction over nickel supported on alumina and lanthana-alumina catalysts, *Int. J. Hydrogen Energy* 42 (2017) 13039–13060.
- [74] Sandun D. Sushil Adhikari, S.D. Fernando, R. Filip, Philip H. Mark Bricka, A. Steele, A Haryanto, Conversion of glycerol to hydrogen via a steam reforming process over nickel catalysts, *Energy Fuels* 22 (2008) 1220–1226.
- [75] M.A. Goula, N.D. Charisiou, P.K. Pandis, V.N. Stathopoulos, A Ni/apatite-type lanthanum silicate supported catalyst in glycerol steam reforming reaction, *RSC Adv.* 6 (2016) 78954–78958.
- [76] N.D. Charisiou, V. Sebastian, S.J. Hinder, M.A. Baker, K. Polychronopoulou, M. A. Goula, Ni catalysts based on attapulgite for hydrogen production through the glycerol steam reforming reaction, *Catalysts* 9 (2019) 650.